คณะวิทยาศาสตร์ มหาวิทยาลัยมหิดล
Faculty of Science, Mahidol University

รายงานวิจัยฉบับสมบูรณ์

โครงการ การศึกษารังสีแกมมาที่มาจากโลกด้วยกล้องโทรทรรศน์อวกาศเฟอร์มี

โดย ดร. วฤทธิ์ มิตรธรรมศิริ

เดือน ปี ที่เสร็จโครงการ
ธันวาคม พ.ศ. 2560

สัญญาเลขที่ TRG5880173

รายงานวิจัยฉบับสมบูรณ์

โครงการ การศึกษารังสีแกมมาที่มาจากโลกด้วยกล้องโทรทรรศน์อวกาศเฟอร์มี

โดย ดร. วฤทธิ์ มิตรธรรมศิริ
ภาควิชาฟิสิกส์ คณะวิทยาศาสตร์
มหาวิทยาลัยมหิดล

สนับสนุนโดยสำนักงานกองทุนสนับสนุนการวิจัย
และ
คณะวิทยาศาสตร์ มหาวิทยาลัยมหิดล

Abstract

Cosmic rays (CRs) are high energy particles in space. The Earth's upper atmosphere is continuously bombarded by CRs, resulting in atmospheric ionization and producing various kinds of secondary particles, including gamma rays. The Earth's magnetic field behaves like a CR spectrometer which allows particles above a certain energy to interact with the atmosphere at a given region. Therefore, the rates of CR-atmosphere interactions, and hence the atmospheric ionization rates and gamma-ray intensities, depend on the geomagnetic field locations. We use the Earth's gamma-ray data observed by the *Fermi* Gamma-ray Space Telescope to indirectly study the CR spectrum, the atmosphere, and the geomagnetic field. The current result is the computer model of the atmospheric ionization due to CRs, which can be compared against other measurements and calculations to verify the validity of our model. We also use the model to evaluate the effects of CRs on airplane passengers' health. Furthermore, the study of Earth's gamma-ray emission has been one of the *Fermi* Collaboration's tools to calibrate and monitor the detector's performance, which is very useful for other studies.

Project Code : TRG5880173

Project Title : Study of Earth's γ-Ray Emission with the *Fermi* Gamma-ray Space Telescope

Investigator : Dr. Warit Mitthumsiri
Department of Physics, Faculty of Science, Mahidol University

E-mail Address : warit.mit@mahidol.ac.th

Project Period : 2 years 6 months (July 2015 – December 2017)

บทคัดย่อ

รังสีคอสมิก คืออนุภาคพลังงานสูงในอวกาศ เมื่ออนุภาครังสีคอสมิกเคลื่อนที่มากระทบกับชั้นบรรยากาศของโลก จะเกิดปฏิกิริยาทำให้อากาศแตกตัว และสร้างอนุภาคย่อยๆ ขึ้นหลายชนิด รวมถึงรังสีแกมมา สนามแม่เหล็กของโลกจะเป็นตัวคัดกรองพลังงานของอนุภาครังสีคอสมิกที่เข้ามายังโลก ทำให้ที่บริเวณต่างๆ กันมีอัตราการเกิดปฏิริยาระหว่างรังสีคอสมิกกับอากาศต่างกัน ส่งผลให้อัตราการแตกตัวของอากาศ และความเข้มของรังสีแกมมาที่บริเวณต่างๆ บนโลกไม่เท่ากัน เราใช้ข้อมูลจากกล้องโทรทรรศน์อวกาศเฟอร์มี เพื่อศึกษารังสีแกมมา จากชั้นบรรยากาศของโลกที่กล่าวมานี้ เพื่อเป็นข้อมูลเกี่ยวกับลักษณะพลังงานของรังสีคอสมิก ชั้นบรรยากาศ และสนามแม่เหล็กของโลก ผลงานในปัจจุบันคือการสร้างแบบจำลองเชิงคอมพิวเตอร์เพื่อสังเกตการแตกตัวของอากาศเนื่องจากปฏิกิริยาระหว่างรังสีคอสมิกและชั้นบรรยากาศ โดยผลที่ได้สามารถถูกนำไปเปรียบเทียบกับผลการวัดหรือคำนวณโดยกลุ่มวิจัยอื่นๆ เป็นการยืนยันความสมจริงของแบบจำลอง และยังสามารถนำมาใช้ประเมินผลกระทบเชิงสุขภาพต่อผู้โดยสารเครื่องบินเนื่องจากรังสีคอสมิกได้อีกด้วย นอกจากนี้ ข้อมูลรังสีแกมมาจากโลกที่เราศึกษา ได้มีส่วนช่วยในการปรับตั้งค่าของอุปกรณ์ ทำให้เป็นประโยชน์ในการศึกษา รังสีแกมมาหรืออนุภาคที่มาจากแหล่งกำเนิดอื่นๆ โดยทีมวิจัยกล้องโทรทรรศน์อวกาศเฟอร์มี

รหัสโครงการ : TRG5880173

ชื่อโครงการ : การศึกษารังสีแกมมาที่มาจากโลกด้วยกล้องโทรทรรศน์อวกาศเฟอร์มี

ชื่อนักวิจัย : ดร. วฤทธิ์ มิตรธรรมศิริ
ภาควิชาฟิสิกส์ คณะวิทยาศาสตร์ มหาวิทยาลัยมหิดล

อีเมล : warit.mit@mahidol.ac.th

ระยะเวลาโครงการ : 2 ปี 6 เดือน (กรกฎาคม 2558 – ธันวาคม 2560)

เนื้อหา :

บทนำ

การศึกษาฟิสิกส์ดาราศาสตร์ในช่วงคลื่นรังสีแกมมาจึงเป็นเรื่องที่น่าสนใจ เนื่องจากรังสีแกมมาเป็นคลื่นแม่เหล็กไฟฟ้าที่มีพลังงานสูงสุด ที่ถูกสร้างด้วยกระบวนการที่เกี่ยวข้องกับฟิสิกส์พลังงานสูงหรือปฏิกิริยานิวเคลียร์ และรังสีแกมมาเดินทางจากแหล่งกำเนิดมายังเครื่องวัดเป็นเส้นตรงโดยไม่ถูกเบี่ยงเบนด้วยสนามแม่เหล็กในจักรวาล จึงทำให้สามารถบอกตำแหน่งของแหล่งกำเนิดได้ กล้องโทรทรรศน์อวกาศเฟอร์มีเป็นอุปกรณ์สำหรับตรวจวัดรังสีแกมมาที่มาจากวัตถุต่างๆ ในท้องฟ้าโดยเป็นความร่วมมือระหว่างหลายประเทศ เช่น สหรัฐอเมริกา อิตาลี ฝรั่งเศส และญี่ปุ่น กล้องเฟอร์มีถูกส่งขึ้นสู่วงโคจรที่ความสูงประมาณ 560 กิโลเมตร ในปี ค.ศ. 2008 และดำเนินการเก็บข้อมูลมาจนถึงปัจจุบัน และจะยังคงทำงานต่อไปตราบเท่าที่อุปกรณ์ยังใช้งานได้

จากมุมมองของกล้องเฟอร์มี โลกของเราเป็นวัตถุที่สว่างที่สุดในรังสีแกมมาเพราะว่าโลกอยู่ใกล้กับเครื่องวัดมาก รังสีแกมมาที่มาจากโลกถูกสร้างขึ้นด้วยกระบวนการหลัก คือ การที่อนุภาคพลังงานสูงในอวกาศ (รังสีคอสมิก) ชนกับโมเลกุลอากาศในระดับความสูงหลายสิบกิโลเมตรแล้วแตกตัวเป็นอนุภาคย่อยบางชนิดที่สลายตัวเป็นรังสีแกมมา ปรากฏการณ์ฟ้าผ่าก็สามารถสร้างรังสีแกมมาได้ นอกจากนั้น หากมีปฏิกิริยานิวเคลียร์เกิดขึ้นที่บรรยากาศชั้นบน เช่น การทดสอบอาวุธนิวเคลียร์ที่ความสูงมากๆ ก็จะเกิดรังสีแกมมาที่สามารถตรวจวัดได้จากเครื่องวัดในอวกาศเช่นกัน

สนามแม่เหล็กของโลกสามารถเบี่ยงเบนอนุภาคที่มีประจุ จึงเป็นตัวคัดกรองพลังงานของอนุภาครังสีคอสมิก ทำให้บริเวณต่างๆ บนโลกมีรังสีคอสมิกที่ปริมาณและพลังงานต่างๆ กันผ่านเข้ามายังบรรยากาศชั้นบน ส่งผลให้อัตราการแตกตัวของอากาศและความเข้มของรังสีแกมมาไม่เท่ากันที่ตำแหน่งต่างกันบนโลก โดยบริเวณเส้นศูนย์สูตรสนามแม่เหล็กเป็นบริเวณที่อนุภาครับสีคอสมิกเข้ามายาก จึงมีอัตราการแตกตัวที่ต่ำกว่าบริเวณขั้วแม่เหล็ก ดังนั้น การรังสีแกมมาจากโลกจะมีประโยชน์ในการศึกษาปฏิกิริยาของอนุภาคในชั้นบรรยากาศ รังสีคอสมิก ชั้นบรรยากาศ สนามแม่เหล็กของโลก และสามารถใช้ทดสอบประสิทธิภาพในการระบุพลังงานของเครื่องวัดได้อีกด้วย

วัตถุประสงค์

1. ศึกษาการเปล่งรังสีแกมมาจากชั้นบรรยากาศของโลก ด้วยข้อมูลจากกล้องโทรทรรศน์อวกาศเฟอร์มี เพื่อสังเกตความเข้มของรังสีแกมมาที่ตำแหน่ง (ละติจูด-ลองจิจูด) ต่างๆ
2. ศึกษาความสัมพันธ์ระหว่างความเข้มของรังสีแกมมากับลักษณะของสนามแม่เหล็กโลก
3. ศึกษาปฏิกิริยาระหว่างรังสีคอสมิกกับชั้นบรรยากาศโลกที่ทำให้เกิดการแตกตัวประจุของอากาศ ซึ่งอาจส่งผลต่อผู้โดยสารเครื่องบิน

4. ใช้ข้อมูลรังสีแกมมาที่มาจากโลกในการทดสอบปรับตั้งค่าประสิทธิภาพของกล้องโทรทรรศน์อวกาศเฟอร์มี ซึ่งจะเป็นประโยชน์ต่อการศึกษาแหล่งกำเนิดรังสีแกมมาอื่นๆ

วิธีทดลอง

เราใช้ข้อมูลรังสีแกมมาที่มาจากโลกที่ถูกตรวจวัดโดยกล้องโทรทรรศน์เฟอร์มี ตั้งแต่ปี ค.ศ. 2008 – 2017 ในช่วงพลังงานประมาณ 500 MeV – 20 GeV เพื่อนำมาเปลี่ยนระบบพิกัด และสร้างแผนที่ความเข้มรังสีแกมมาที่ตำแหน่งต่างๆ (ละติจูด-ลองจิจูด) บนโลก และนำมาเปรียบเทียบกับแบบจำลองของสนามแม่เหล็กของโลก เพื่อสังเกตความสัมพันธ์ระหว่างลักษณะของสนามแม่เหล็กและความเข้มของรังสีแกมมาที่วัดได้

นอกจากนี้เราได้สร้างแบบจำลองเชิงคอมพิวเตอร์ของปฏิกิริยาระหว่างอนุภาครังสีคอสมิกกับชั้นบรรยากาศโลก ด้วยโปรแกรม FLUKA โดยใช้ข้อมูลจริงที่ถูกวัดได้ด้วยดาวเทียมอุตุนิยมวิทยา เพื่อคำนวณอัตราการแตกตัวประจุของอากาศและนำไปเปรียบเทียบกับผลการวัดหรือการจำลองจากกลุ่มวิจัยอื่น นอกจากนี้ แบบจำลองยังสามารถถูกใช้เพื่อประมาณปริมาณรังสีที่ระดับความสูงประมาณ 12 กิโลเมตรจากระดับน้ำทะเล ซึ่งเป็นความสูงทั่วไปของเครื่องบินพาณิชย์ ทำให้สามารถประเมินผลกระทบต่อผู้โดยสารเครื่องบินอันเนื่องมาจากรังสีคอสมิกได้

ผลการทดลอง

ผลที่ต้องการในระยะยาว จะเป็นภาพของโลกในช่วงคลื่นรังสีแกมมาภาพแรกที่จะให้ข้อมูลสำคัญเกี่ยวกับสนามแม่เหล็กโลก รังสีคอสมิก ชั้นบรรยากาศ และอื่นๆ อีกมาก ในรูปแบบการวิเคราะห์ที่ไม่เคยมีใครทำมาก่อน นอกจากนี้การสร้างแบบจำลองการปล่อยรังสีแกมมาของโลกได้เป็นประโยชน์ต่อทีมวิจัยของกล้องโทรทรรศน์อวกาศเฟอร์มีในหลายด้าน เนื่องจากความสว่างอันมหาศาลของโลกในช่วงรังสีแกมมากลายเป็นสัญญาณรบกวนการศึกษาวัตถุเชิงดาราศาสตร์อื่นๆ ในท้องฟ้า การมีแบบจำลองรังสีแกมมาจากโลกที่ดี จะช่วยให้นักวิจัยเข้าใจและหักลบสัญญาณรบกวนนี้ได้อย่างละเอียดและมีประสิทธิภาพขึ้น โดยเฉพาะเมื่อต้องการศึกษาแหล่งกำเนิดที่สว่างน้อยและมีพลังงานต่ำ ไม่เพียงเท่านั้น รังสีแกมมาจากโลกยังมีความสำคัญต่อการปรับและตั้งค่าเชิงพลังงานและประสิทธิภาพของกล้องเฟอร์มีมาตลอด การศึกษานี้มีประโยชน์ต่องานวิจัยแทบทุกด้านของทีมวิจัย

ผลผลิตในปัจจุบันคือ ผลการจำลองเชิงคอมพิวเตอร์ของปฏิกิริยาระหว่างรังสีคอสมิกที่มาจากดวงอาทิตย์กับชั้นบรรยากาศ ซึ่งทำให้เกิดการแตกตัวประจุของอากาศ โดยทำการศึกษาเหตุการณ์การปะทุครั้งใหญ่มากของดวงอาทิตย์ในปี 2005 เพื่อสังเกตการณ์แตกตัวประจุ และปริมาณรังสีที่ชั้นความสูงต่างๆ ในบรรยากาศ ทำให้สามารถประเมินผลกระทบต่อสุขภาพของผู้โดยสารเครื่องบินที่ได้รับรังสีจากเหตุการณ์นี้ได้ โดยพบว่า อัตราการแตกตัวของอากาศที่เกิดจากรังสีคอสมิกจากกาแลกซีที่เราคำนวณได้ มีความสอดคล้องกับผลการวัดจริงโดยใช้บอลลูน และผลจากการคำนวณโดยกลุ่มวิจัยอื่น ปริมาณรังสีมากที่สุดอันเนื่องมาจากดวง

อาทิตย์ที่เกิดขึ้นบริเวณขั้วโลกใต้จะทำให้ผู้โดยสารเครื่องบินได้รับรังสีในอัตราที่มากกว่าสภาวะปกติที่ระดับน้ำทะเลประมาณ 10,000 เท่า ถึงแม้ว่าการปะทุนี้ใช้เวลาเพียงประมาณ 1-2 ชั่วโมง ทำให้ปริมาณรังสีโดยรวมทั้งเหตุการณ์ยังไม่เกินค่าที่แนะนำโดยรวมทั้งปีโดยองค์กรสากลที่เกี่ยวข้องกับอันตรายจากกัมมันตรังสี แต่การได้รับรังสีปริมาณมหาศาลในระยะเวลาสั้นๆ (ปริมาณรังสีปกติที่ระดับน้ำทะเลทั้งปี ในเวลาเพียง 1 ชั่วโมง) ก็ยังอาจทำให้เกิดผลข้างเคียงได้ ผลงานชิ้นนี้ยังเป็นการเริ่มต้นสร้างแบบจำลองของชั้นบรรยากาศ และการทำปฏิกิริยากับรังสีคอสมิก ที่สามารถนำไปเปรียบเทียบและพัฒนาต่อไปได้

สรุปและวิจารณ์ผลการทดลอง

การศึกษาการเปล่งรังสีแกมมาจากโลกยังคงดำเนินต่อไป โดยเบื้องต้นได้แผนภาพของโลกในช่วงคลื่นรังสีแกมมา และสามารถนำมาเปรียบเทียบกับแบบจำลองของสนามแม่เหล็กได้แล้ว โดยความสัมพันธ์กับลักษณะของสนามแม่เหล็กเป็นไปตามที่คาด คือบริเวณและทิศทางที่สนามแม่เหล็กคัดกรองเฉพาะรังสีคอสมิกพลังงานสูง จะมีความเข้มของรังสีแกมมาน้อยเนื่องจากรังสีคอสมิกที่มีพลังงานสูงมีจำนวนน้อย อย่างไรก็ตาม ลักษณะพลังงานของรังสีแกมมาที่ได้ยังไม่ตรงกับผลจากการศึกษาของทีมวิจัยกล้องโทรทรรศน์อวกาศเฟอร์มีในอดีต จึงยังคงต้องตรวจสอบต่อไป

สำหรับการสร้างแบบจำลองปฏิกิริยาระหว่างรังสีคอสมิกกับชั้นบรรยากาศ ผลที่ได้มีความสอดคล้องกับผลที่กลุ่มวิจัยอื่นๆ ได้เคยทำไว้ ทั้งเชิงการทดลองและการจำลอง และทั้งอัตราการแตกตัวของอากาศอันเนื่องมาจากรังสีคอสมิกในกาแลกซี และรังสีคอสมิกจากดวงอาทิตย์ จึงเป็นสิ่งยืนยันถึงความถูกต้องของแบบจำลองของเราในเบื้องต้น ที่จะสามารถนำไปใช้เพื่อศึกษาปฏิกิริยาระหว่างรังสีคอสมิกกับอากาศได้ละเอียดยิ่งขึ้น

ข้อเสนอแนะสำหรับงานวิจัยในอนาคต

ต้องหาสาเหตุที่ทำให้ลักษณะพลังงานของรังสีแกมมาจากโลกที่ได้จากการวิเคราะห์ในแบบปัจจุบันไม่สอดคล้องกับการศึกษาในอดีต โดยพยายามปรับเปลี่ยนวิธีการคำนวณและช่วงเวลาของข้อมูลที่ใช้ให้ใกล้เคียงกับวิธีในอดีตให้มากที่สุด โดยแบบจำลองเชิงคอมพิวเตอร์ของชั้นบรรยากาศที่ได้สร้างขึ้นอาจจะนำมาช่วยได้ และควรนำแบบจำลองที่ได้ไปต่อยอดการศึกษาเกี่ยวกับรังสีคอสมิกและชั้นบรรยากาศต่อไป

Keywords : Ionization, radiation dose, Earth’s gamma ray, cosmic rays, geomagnetic field

คำหลัก : การแตกตัวประจุ ปริมาณรังสี รังสีแกมมาจากโลก รังสีคอสมิก สนามแม่เหล็กโลก

Output จากโครงการวิจัยที่ได้รับทุนจาก สกว.

1. ผลงานตีพิมพ์ในวารสารวิชาการนานาชาติ (ระบุชื่อผู้แต่ง ชื่อเรื่อง ชื่อวารสาร ปี เล่มที่ เลขที่ และหน้า) หรือผลงานตามที่คาดไว้ในสัญญาโครงการ
   - **1.1** **W. Mitthumsiri**, A. Seripienlert, U. Tortermpun, P.-S. Mangeard, A. Sáiz, D. Ruffolo, R. Macatangay, “Modeling polar region atmospheric ionization induced by the giant solar storm on 20 January 2005” J. Geophys. Res. Space Physics, 122, 7946-55 (2017) (Impact Factor 3.44)
   - **1.2** S. Abdollahi, et al. (Fermi-LAT Collaboration), “Cosmic-ray electron-positron spectrum from 7 GeV to 2 TeV with the Fermi Large Area Telescope” Phys. Rev. D, 95, 082007 (2017) (Impact Factor 4.557)

2. การนำผลงานวิจัยไปใช้ประโยชน์
   เชิงวิชาการ (มีการพัฒนาการเรียนการสอน/สร้างนักวิจัยใหม่)
   - **2.1** การศึกษารังสีแกมมาจากโลก ทำให้กลุ่มวิจัยเฟอร์มีนำไปปรับตั้งค่าและตรวจสอบประสิทธิภาพในการวัดพลังงานของอุปกรณ์ ทำให้มีประโยชน์ในการวิเคราะห์ศึกษาข้อมูลที่มาจากแหล่งกำเนิดอื่นๆ อีกมาก
   - **2.2** มีนักศึกษาปริญญาโทและเอกอย่างละ 1 คน ที่ได้เข้ามาฝึกทำวิจัยในหัวข้อนี้ และได้มีโอกาสไปนำเสนอผลงานที่งานประชุมวิชาการ เมืองซานฟรานซิสโก และไปทำวิจัยที่มหาวิทยาลัยสแตนฟอร์ด ประเทศสหรัฐอเมริกา รวมถึงนำเสนอผลงานที่งานประชุมวิชาการในประเทศอีกด้วย

3. อื่นๆ (เช่น ผลงานตีพิมพ์ในวารสารวิชาการในประเทศ การเสนอผลงานในที่ประชุมวิชาการ หนังสือ การจดสิทธิบัตร)
   - **3.1** S. Madlee, **W. Mitthumsiri**, “Earth’s gamma-ray emission in geographical coordinates with Fermi-LAT data,” Siam Physics Congress 2016, 8-10 Jun 2016, Ubon Ratchathani, Thailand (oral)
   - **3.2** S. Madlee, **W. Mitthumsiri**, S. Digel, D. J. Ruffolo, “Gamma-ray emission of the Earth’s upper atmosphere in geographical coordinates with Fermi-LAT,” AGU Fall Meeting 2016, 12-16 Dec 2016, San Francisco, USA (poster)
   - **3.3** N. Thanapreechanan, “Search for Galactic dark matter from γ–ray spectral lines with Fermi-LAT data” J. of Physics: Conf. Series, 901, 012002 (2017) (oral and proceeding)

AGU PUBLICATIONS

JGR

Journal of Geophysical Research: Space Physics

RESEARCH ARTICLE

10.1002/2017JA024125

Key Points:

- We model polar region tropospheric ionization and radiation dosage from the 20 January 2005 solar storm in 1 min steps during 6:50-8:00 UT
- Our methods, based on neutron monitor data, account for the time-dependent relativistic solar ion spectrum and anisotropy
- The most severe radiation dose an airplane passenger could have been exposed to during this event is ∼0.75 mSv

Supporting Information:

- Supporting Information S1
- Figure S1
- Movie S1
- Movie S2

Correspondence to:
D. Ruffolo,
david.ruf@mahidol.ac.th

Citation:
Mitthumsiri, W., A. Seripienlert, U. Tortermpun, P.-S. Mangeard, A. Sáiz, D. Ruffolo, and R. Macatangay (2017), Modeling polar region atmospheric ionization induced by the giant solar storm on 20 January 2005, *J. Geophys. Res. Space Physics*, *122*, 7946–7955, doi:10.1002/2017JA024125.

Received 14 MAR 2017
Accepted 28 JUL 2017
Accepted article online 2 AUG 2017
Published online 26 AUG 2017

Modeling polar region atmospheric ionization induced by the giant solar storm on 20 January 2005

W. Mitthumsiri[1], **A. Seripienlert**[2,3,4], **U. Tortermpun**[1,3], **P.-S. Mangeard**[1,3,5], **A. Sáiz**[1], **D. Ruffolo**[1], **and R. Macatangay**[3]

[1]Department of Physics, Faculty of Science, Mahidol University, Bangkok, Thailand, [2]Division of Physics, Faculty of Science and Technology, Rajamangala University of Technology Thanyaburi, Pathum Thani, Thailand, [3]National Astronomical Research Institute of Thailand, Chiang Mai, Thailand, [4]Now at Dacon Inspection Services Co., Ltd., Rayong, Thailand, [5]Now at Department of Physics and Astronomy, University of Delaware, Newark, Delaware, USA

Abstract Ionization in Earth's troposphere is mainly due to Galactic cosmic rays. Occasionally, solar storms produce intense relativistic ion beams that significantly increase such ionization. One of the largest recorded solar radiation storms, on 20 January 2005, resulted in up to 55-fold increases in the count rates of ground-based particle detectors in polar regions. We use McMurdo and Inuvik neutron monitor data to estimate accurate time profiles of ion energy spectra above the atmosphere at each location. Using data-driven atmospheric models, we perform Monte Carlo simulations of particle-air interactions and calculate atmospheric ionization and potential biological dosage versus altitude and time for each location. We found that if airplane passengers had traversed the south polar region, they could have been exposed to the typical annual cosmic radiation dosage at sea level within 1 h. These techniques can help evaluate possible influences of solar activity on atmospheric properties.

1. Introduction

There is a variety of "space weather" effects on human activity due to high-speed solar wind streams and solar storms, including those associated with solar energetic particles (SEPs). While humans at Earth are usually well protected by Earth's magnetic field and atmosphere, there are occasional solar storms that produce SEPs of sufficient energy and intensity to shower in the atmosphere and significantly enhance the flux of ionizing radiation above the background level due to Galactic cosmic rays (GCRs), for which the flux decreases less rapidly with energy. Higher in the atmosphere, the less energetic SEPs have a relatively stronger contribution to the ionizing radiation. Even at ground level, neutron monitors (NMs), as the ground-based detectors that are most sensitive to relatively low energy cosmic rays (CRs), can sometimes detect SEPs. Such events of solar origin are known as ground level enhancements (GLEs).

Potential space weather hazards for air travelers and aircraft electronics are closely related to atmospheric ionization, as both are due to ionizing radiation from atmospheric showers. Historically, the first GLE was discovered by Forbush in February 1942 [*Forbush*, 1946]. Later, enhanced atmospheric ionization at altitudes above 30 km was observed during the giant GLE of 23 February 1956 [*Dorman*, 1963, 2004]. Modern measurements of atmospheric ionization [e.g., *Bazilevskaya et al.*, 2008] can provide a reality check on calculations. Furthermore, atmospheric ionization is important to the formation and development of condensation nuclei for aerosols [*Mironova et al.*, 2012]. Some simulation studies suggest significant contributions from GCRs to the atmospheric chemical composition in the stratosphere and troposphere, especially near the polar regions, by enhancing the production of NO_x and HO_x [e.g., *Calisto et al.*, 2011]. Hypothetically, these molecules have measurable impacts on the amount of ozone which consequently affects the tropospheric temperature and wind flow. Thus, the present study aims to estimate the distribution of ionization and radiation dosage in the lower atmosphere (up to 25 km) as expected from a large GLE to provide more information about the connections between CRs and the various phenomena mentioned above.

The giant GLE of 20 January 2005 was the strongest event in the past 60 years, and relativistic solar particle fluxes were well measured by polar NMs, including the *Spaceship Earth* network [*Bieber et al.*, 2013]. The CR flux

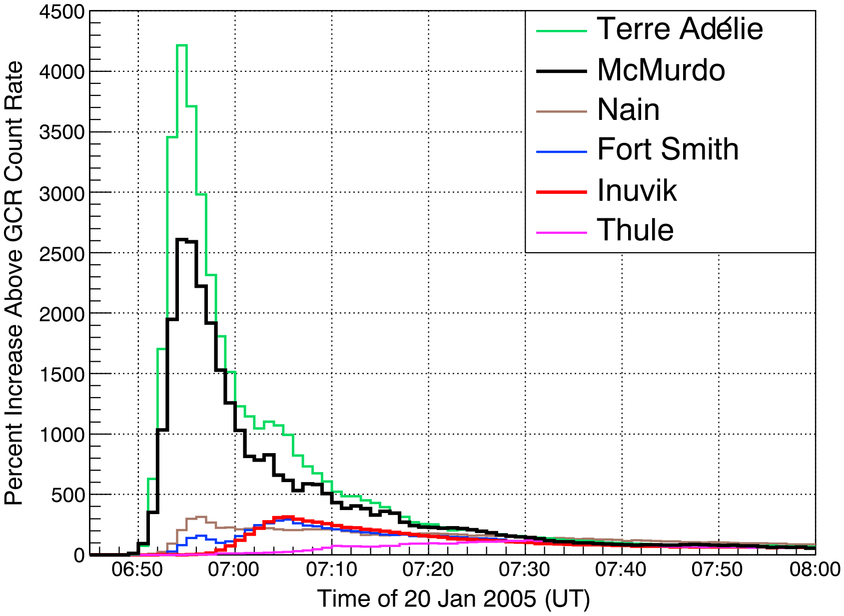

Figure 1. One minute averaged percent increases of count rates, above the background rate produced by Galactic cosmic rays (GCRs), from six polar region neutron monitor (NM) stations due to the giant solar radiation storm on 20 January 2005 (replotted from *Bieber et al.* [2013]). McMurdo and Inuvik data are emphasized in this work.

as measured by the high-altitude South Pole NM increased by ≈5500%. Fortunately, such high increases occurred only at or near Antarctica, with no commercial air travel; this event highlights the potential effects on polar air flights when such increases occur over the north polar region in the future. With such a large increase in particle fluxes, this event provides a good example case for estimating atmospheric ionization [*Mishev et al.*, 2012] and radiation dosage [*Bütikofer and Flückiger*, 2011; *Mishev*, 2014; *Mishev et al.*, 2015]. Here we make direct use of accurate measurements by NMs of the time-dependent particle flux at different locations, combined with detailed Monte Carlo simulations based on the estimated atmospheric structure at those locations and times, to precisely estimate atmospheric ionization and radiation dosage due to relativistic solar particles as a function of altitude and time.

2. Methods

2.1. Neutron Monitor Data

When CRs strike the upper atmosphere, showers of secondary particles, including neutrons, are produced and can be detected by NMs on the ground. An important advantage of NMs is a high detection rate, allowing precise measurement of secondary neutron count variation in a relatively short (e.g., 1 min) time interval. We can use the NM count rate data to obtain information about the CR spectrum at the top of the atmosphere as a function of time. This is discussed in detail in section 2.2.

For a given location on Earth, only CRs above a certain rigidity (momentum per charge) can penetrate the Earth's magnetic field to interact with the atmosphere. This geomagnetic cutoff rigidity varies from ≈17 GV in and near Thailand to ≲0.01 GV near the geomagnetic poles, where there is an atmospheric cutoff of ∼1 GV for CR showers to register counts in ground-based NMs. Therefore, NM stations at different locations are sensitive to different rigidity ranges of the CR spectrum. SEPs, predominantly relativistic protons and alpha particles, can have a rigidity up to ∼10 GV and may arrive to Earth mostly near the polar regions, resulting in increases of NM count rates above the background GCR count rates. On 20 January 2005 starting from 6:50 UT, a major GLE was observed near the polar regions. Satellite instruments also clearly registered this event with enormous increases of particle fluxes and significant changes of spectral parameters. Percent increases of selected polar region NM count rates of this GLE are shown in Figure 1.

Near the start of this GLE, as shown in Figure 1, there was a very strong anisotropy in the solar particle flux, with a ratio of flux arriving near the South Pole to that near the North Pole of over 1000:1 at 6:54 UT, and the anisotropy became much weaker in the later (decay) phase of the event [*Bieber et al.*, 2013]. At times of strong anisotropy, remote satellite data may not provide accurate particle fluxes above specific locations of interest. We therefore use NM count rate data, specifically from low-cutoff stations at McMurdo (77.9°S 166.6°E, in Antarctica) and Inuvik (68.4°N 133.7°W, in Canada), to calculate the time-dependent CR spectra above the atmosphere at those locations. As shown in Figure 1, NM data from Terre Adélie and Thule during this GLE event could represent two opposite ends of the extreme cases, while data from McMurdo and Inuvik are good base-case scenarios for the south and north polar regions, enabling us to compare our results against those from other studies more consistently. Furthermore, an important motivation to study the location at Inuvik station is the dense air traffic in that region, for relevance to the actual health effects on airline passengers.

2.2. Estimations of GCR and SEP Spectra

GCR Spectra. The solar cycle effects known as solar modulation can affect GCRs up to ~30 GV and are known to follow a cycle of about 11–12 years. We use the parameterization of the local GCR proton spectrum from *Usoskin et al.* [2011a], taking into account the solar modulation effect for this specific event by putting in the force field potential $\phi = 1188$ MV as estimated for 20 January 2005 [*Usoskin et al.*, 2011b]. As recommended by *Usoskin et al.* [2011a], we model the contribution of ions with $Z \geq 2$, which we call "heavy ions," as if they were alpha particles with a flux of number of nucleons equal to 30% of the proton flux. Our trajectory simulations using the 11th generation International Geomagnetic Reference Field and the method of *Lin et al.* [1995] indicate that during times of interest, the vertical geomagnetic cutoff rigidity was below about 10 MV, a rigidity range where particles generate negligible ionization below 25 km in altitude. Therefore, we do not implement a geomagnetic cutoff at McMurdo or Inuvik. For the timescale of a few hours in this study, it is sufficient to approximate that the GCR fluxes are constant in time and isotropic.

SEP Spectra. The SEP spectra of this GLE are more complicated to model. The SEP-induced ionization of the lower atmosphere is dominated by GeV range particles, so we stress an accurate representation of the time dependence of SEP spectra in this high-energy range. The time variation of the GeV range SEP flux is measured precisely at NM stations, and as described earlier we estimate the SEP fluxes at McMurdo, Antarctica, and Inuvik, Canada, based on the near-sea level NM count rates there.

We use NM count rates only to estimate the time-dependent amplitudes of the SEP spectra; the spectral shapes are as estimated below. To justify the use of local NM count rates to determine the time-dependent amplitudes of the SEP spectra at each location, we note that our calculation of the median kinetic energy of primary cosmic rays, in terms of their contribution to either atmospheric ionization or radiation dosage at 12 km altitude above either McMurdo or Inuvik, ranges between 0.8 and 1.4 GeV, in comparison with the median kinetic energy of protons contributing to the NM count rate of 1.40 GeV [*Bieber et al.*, 2013]. Furthermore, because of magnetic mirroring along the converging magnetic field lines near Earth's poles, a wide range of particle arrival directions at a given rigidity maps to a narrow range of asymptotic directions in space. For example, we calculate that for the median rigidity for either NM station, arrival directions at zenith angle 30°, i.e., over a circle of diameter 60°, map into asymptotic directions over an oval of diameter ~3°. Thus, the primary cosmic ray directions contributing to the NM count rate are very similar to those contributing to atmospheric ionization and radiation dosage at aircraft altitude.

Regarding the SEP spectral shape, the rigidity spectral index of SEPs during the GLE of 20 January 2005 was measured minute by minute using the count rate ratio of bare neutron counters to the NM at the South Pole [*Bieber et al.*, 2013]. These two detector systems have different energy sensitivity so their ratio can be used to roughly estimate the spectral index [*Bieber and Evenson*, 1991]. This method has been used to study the spectral index of various GLEs [*Bieber et al.*, 2002; *Sáiz et al.*, 2008] and gave very similar results to an independent method based on data for many NMs [*Cramp et al.*, 1997] for the GLE of 22 October 1989 [*Ruffolo et al.*, 2006]. Because the SEP spectral index reported by *Bieber et al.* [2013] for 20 January 2005 was measured with 1 min resolution over the narrow rigidity range of ~1 to 5 GV as sampled by polar NMs, it is the most relevant determination of the spectral index for the present study. (That work also contains a summary of widely varying estimates of the spectral index for that event, for different or broader ranges of rigidity and coarser time resolution.) *Bieber et al.* [2013] found that the apparent spectral index γ over that rigidity range was ~3 at the the onset at 0649 UT but rapidly increased (softened) to nearly 5 by 0653 UT. The spectrum was initially hard because the most energetic particles arrived first, but it quickly softened due to velocity dispersion. There was another dip to a lower (harder) spectral index at 0655 UT due to a second dispersive injection peak. Afterward, the spectrum gradually became softer to approach a steady state with $\gamma = 5.0$. An attractive physical interpretation is that the acceleration of particles near the Sun, of short duration, produced an SEP distribution with a spectral index of 5.0 over this rigidity interval and that the apparent spectral index as observed at Earth was lower (harder) immediately after each injection because many lower energy particles had not arrived yet. This interpretation is supported by Figure 4 of *Bieber et al.* [2013], which compares the spectrum at a polar NM with the proton spectrum measured by the GOES spacecraft at lower energies, and shows that the GOES spectrum was initially much lower than the NM spectral trend and then caught up to it at later times. (Note that *Mewaldt et al.* [2005] consider that the GOES proton data channels above 200 MeV are difficult to reconcile with a smooth extrapolation of the spectra observed below 100 MeV and therefore do not make use of such data; if such data are removed from Figure 4 of *Bieber et al.* [2013], the data are indeed easier to understand in terms of velocity dispersion.)

To model this dispersive onset, we implement a simple time-varying cutoff at low energy; recall that our estimates of ionization and radiation dosage below an altitude of 25 km are most sensitive to GeV range particles. The time-dependent p and He energy spectra are described by a power law in rigidity with the constant spectral index of 5.0 and a low-energy cutoff T_c

$$\frac{\mathrm{d}N}{\mathrm{d}}R = I_0(t)\left(\frac{R_0}{R(T)}\right)^5 \exp\left(\frac{T_c}{T_c(t)-T}\right) \text{ for } T > T_c(t), \qquad (1)$$

where N is particle intensity (number of particles per unit area, per unit time, and per unit solid angle), T is kinetic energy per nucleon, R is rigidity, and t is time. Here I_0 is the spectral amplitude, which depends on the (arbitrary) choice of reference rigidity, R_0.

With the spectral shape determined in this way, the remainder of this subsection describes how we use the precisely measured NM count rate at each station during each 1 min interval to infer the *amplitude* I_0 of the proton and heavy ion spectra for that minute.

In order to extract the SEP spectra from NM count rates, we use results from an analysis of data from a latitude survey [*Nuntiyakul et al.*, 2014], which was performed by carrying an NM on a ship across a wide range of geographical locations with widely varying geomagnetic cutoff rigidity between October 2004 and April 2005. This provides a measured combined response function of sea level NMs to all GCR particle types around January 2005 as a function of rigidity.

Next, we employ the local GCR proton and heavy ion (with He + heavy ions modeled as additional He) spectral models from *Usoskin et al.* [2011a] as previously described. Using the average solar modulation potential during the period of interest ($\phi = 636.3$ MV between October 2004 and April 2005; see http://cosmicrays.oulu.fi/phi/Phi_mon.txt) along with the parameterized ratio of He to p yield functions at varying rigidity from *Caballero-Lopez and Moraal* [2012], we obtain the NM yield functions for p and He separately, for which the values are shown in Table S1 in the supporting information and a comparison with some other yield functions in the literature is shown in Figure S1 in the supporting information. Our yield functions based on latitude survey data can then be used to calculate the SEP p and heavy ion spectra above McMurdo and Inuvik NM stations from the measured percentage increases of NM count rates (over the GCR background) under these assumptions.

1. The yield functions for the shipborne NM in the latitude survey [*Nuntiyakul et al.*, 2014] are used for the McMurdo and Inuvik NM, which is reasonable given that they use the same NM64 design and were all near-sea level. Differences in pressure and atmospheric properties at different locations affect the yield functions at the level of a few percent and are negligible compared to other uncertainties.
2. The low-energy cutoff of the spectra $T_c(t)$ decreases with time, depending on the arrival of particles with different velocities traversing a distance of 1.029 AU along the mean interplanetary magnetic field following the Archimedean spiral for the measured solar wind speed of about 800 km s^{-1} starting from injection at ≈2 solar radii. Particles with $T > 1$ GeV nucleon^{-1} started to arrive at 6:50 UT (see top left panel of Figure 4 in *Bieber et al.* [2013]). This simple form of the low-energy cutoff is derived for an instantaneous injection of particles at the distance of 0.01 AU from the solar center. Given that the low-energy cutoff very rapidly decreases to below 100 MeV, as can be seen in the supporting information, and particles at such low energies have very little effect on the ionization and dosage below 25 km, we consider these approximations to be justified and to have very little effect on the results.
3. The SEP He/p ratio for this event is 0.044 at 1.4 GeV/n, which is obtained from fitting the highest-energy data sets for He (20–60 MeV/n) and p (20–400 MeV/n) fluence spectra in *Mewaldt* [2006] and extrapolating

the fits to 1.4 GeV/n, the SEP proton median energy for polar NM observations during this event. The extrapolation is needed because only GeV range SEPs contribute significantly to the atmospheric ionization below ~25 km altitude. It is even more challenging to quantify the GeV range SEP heavy ion composition, so we assume the same relative fractional contribution of ions with $Z > 2$ as for GCR (~50% of He). This gives the (heavy ion)/p ratio of 0.066 at 1.4 GeV/n, the number used in this study. This ratio is likely time and location dependent, but due to the lack of measured GeV data, it is impossible to precisely model it. We therefore assume that the ratio is constant in time and is the same for both McMurdo and Inuvik. By analyzing measurements at lower energies, we estimate the uncertainty of this ratio in the GeV range to be ~20% and observe that varying this ratio by ±20% results in roughly ∓5% changes in the calculated ionization, indicating a small impact from the uncertainty of this ratio.

We have checked the validity of our calculated NM yield functions due to GCR protons and heavy ions as follows. We compute that, at McMurdo and Inuvik, ~40% of NM counts are produced by ions heavier than protons, which is reasonable compared to other estimations from the literature, such as 33% by *Caballero-Lopez and Moraal* [2012] (sea level, 1.0 GV rigidity cutoff) and 51% by *Maurin et al.* [2015] (at 10 GV). Note that this fraction depends on numerous factors such as atmospheric depth, cutoff rigidity, and solar modulation. We also tested using simulation-based NM yield functions at sea level for p and He from *Mangeard et al.* [2016b], which are significantly higher than ours between 1 and 10 GV (see Figure S1 in the supporting information). We then obtain a lower SEP spectral amplitude and understandably obtain ionization rates that are lower than the results shown here by ~35%. Those authors pointed out that FLUKA simulations such as theirs overestimate the yield function below 7 GV when compared with other estimates, and the SEP flux is concentrated at such lower rigidities, so we instead use our yield functions based on latitude survey data and claim ~35% uncertainty in the resulting ionization due to the choice of NM yield functions.

2.3. Monte Carlo Simulations of Atmospheric Ionization

Realistic models of Earth's atmosphere for McMurdo and Inuvik are created with meteorological data from the Global Data Assimilation System (GDAS; see https://www.ready.noaa.gov/gdas1.php) below ~25 km altitude and from NRLMSISE [*Picone et al.*, 2002] above that. The GDAS database provides average atmospheric properties (e.g., humidity, density, pressure, and temperature) from actual measurements between 6:00 and 12:00 UT, while the NRLMSISE model is averaged monthly. Our atmospheric models are composed of 0.25 km thick layers from the altitude of each NM up to ~70 km. More details can be found in Appendix A of *Mangeard et al.* [2016a]. As noted in section 2.2, the primary cosmic ray directions contributing to the NM count rate are very similar to those contributing to atmospheric ionization and radiation dosage at aircraft altitudes and that range of directions is quite narrow [see *Bieber et al.*, 2013, Figure 2], so we neglect effects of differences in the SEP flux over that narrow range.

We use the FLUKA 2011 package [*Ferrari et al.*, 2005; *Böhlen et al.*, 2014] to perform the simulations of atmospheric ionization. GCR and SEP particles with energy spectra described in section 2.2 are simulated to interact with the modeled atmosphere. For both GCRs and SEPs, we apply no geomagnetic rigidity cutoff at either McMurdo or Inuvik. The exact value does not significantly affect the result because showers from low-energy particles have a negligible effect on atmospheric ionization at altitudes of interest (below 25 km). In 1 min time steps during 6:50–8:00 UT, the energy deposited in each atmospheric layer is recorded and converted into an ionization rate using the average ionization potential of air of 35 eV [*Porter et al.*, 1976], a value that was also used by *Mishev et al.* [2012]. The radiation equivalent dose for each layer is also recorded using FLUKA's "DOSE-EQ" default option which provides particle fluences convoluted with conversion factors for different types of particles. The ambient dose equivalent conversion data are from the International Commission on Radiological Protection [*ICRP*, 1996]. Therefore, we obtain the ionization and equivalent dose rate as a function of altitude at any given time between 6:50 and 8:00 UT. We show results up to only 25 km altitude because of the uncertainties in the determination of lower energy CR fluxes which strongly affect the calculations at high altitude but have negligible effects below 25 km.

Atmospheric ionization and radiation dosage from this specific event have been studied by *Mishev et al.* [2012, 2015] and at higher altitudes by *von Savigny et al.* [2007], using space-based CR spectral data and a different simulation method for various geographical locations. The present analysis is complementary to previous studies because it is based on detailed temporal measurements from NMs at specific locations, to precisely specify the time evolution of atmospheric ionization and radiation dosage as a function of altitude.

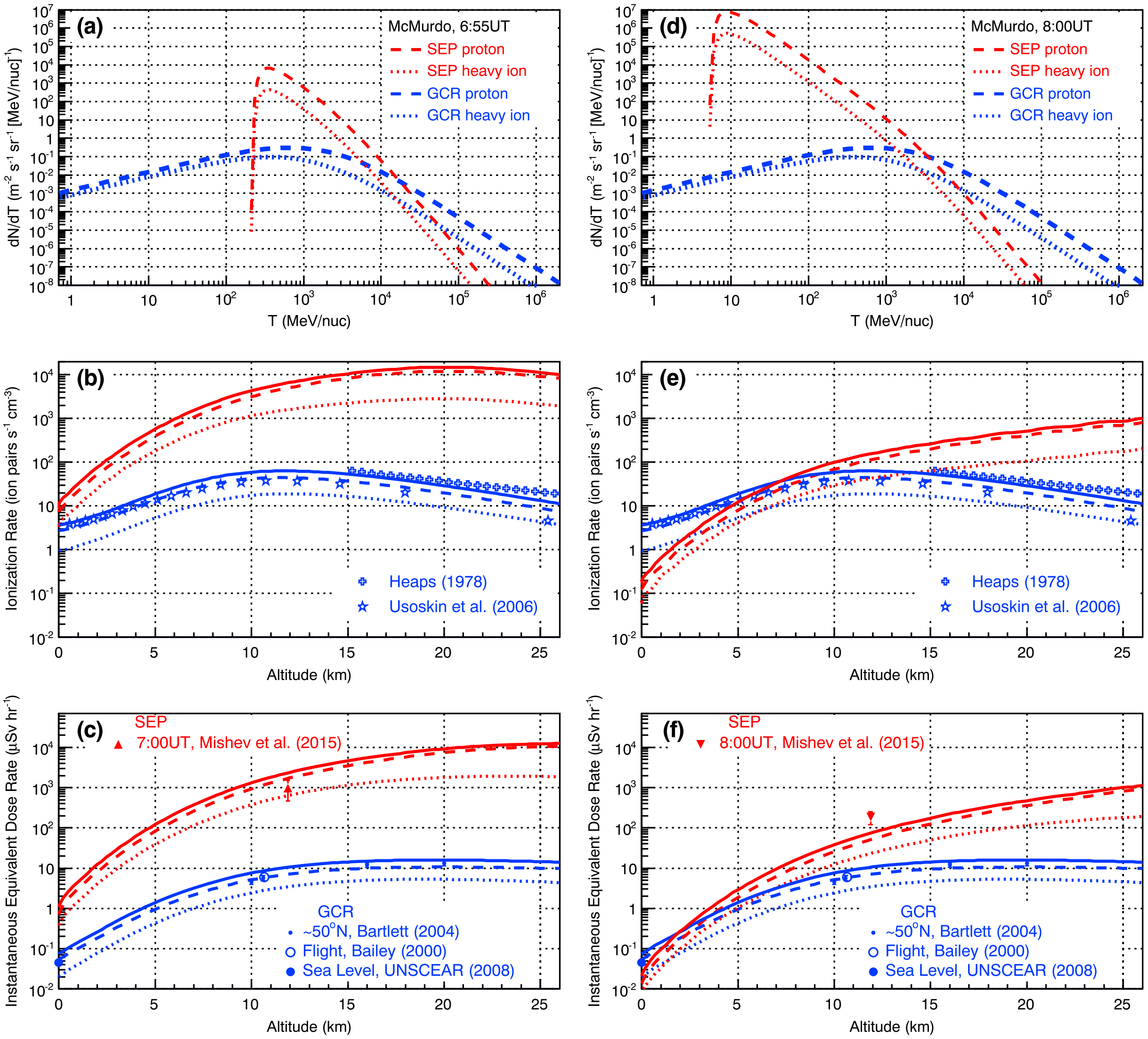

Figure 2. (a, d) Modeled cosmic ray spectra used as inputs to simulate the (b, e) atmospheric ionization production rate and (c, f) instantaneous equivalent dose rate above McMurdo (Antarctica) NM station at the peak time of the GLE of 20 January 2005 (Figures 2a–2c) and a time during the decay phase (Figures 2d–2f). Here the blue and red lines or symbols are associated with GCRs and solar energetic particles (SEPs), respectively. An animation of these graphs as a function of time throughout the event is included in the supporting information.

3. Results and Discussion

Results from simulations for selected times are shown in Figure 2 for McMurdo and Figure 3 for Inuvik. Results for all times are included in the supporting information. Figures 2a–2c and 3a–3c are at the (local) GLE peak time, while Figures 2d–2f and 3d–3f are during the GLE decay phase. The peak times of the SEP fluxes above McMurdo and Inuvik are different: 6:55 UT at McMurdo and 7:06 UT at Inuvik. Estimated SEP and GCR spectra are shown in Figures 2a and 2d and 3a and 3d. Our estimated SEP flux is comparable to that of GCRs near ~10 GeV nucleon^{-1} during the peak of the NM count rate at each location. Our inferred SEP proton flux around ~600 MeV at 6:55 UT above McMurdo is similar to that measured by the Geostationary Orbit Environment Satellite (GOES) [see, e.g., *Matthiä et al.*, 2009, Figure 7] considering the instrumental energy bin and extreme anisotropy for this event.

Results of atmospheric ionization production rates are shown in Figures 2b and 2e and 3b and 3e. We first consider the total ionization rate at about 12 km above sea level, which is a typical altitude for commercial aircraft. Near the peak time, the ionization rate from SEPs at McMurdo is greater than that from GCRs by ~2 orders of magnitude, whereas at Inuvik, the ionization rate from SEPs is greater than that from GCRs by an order

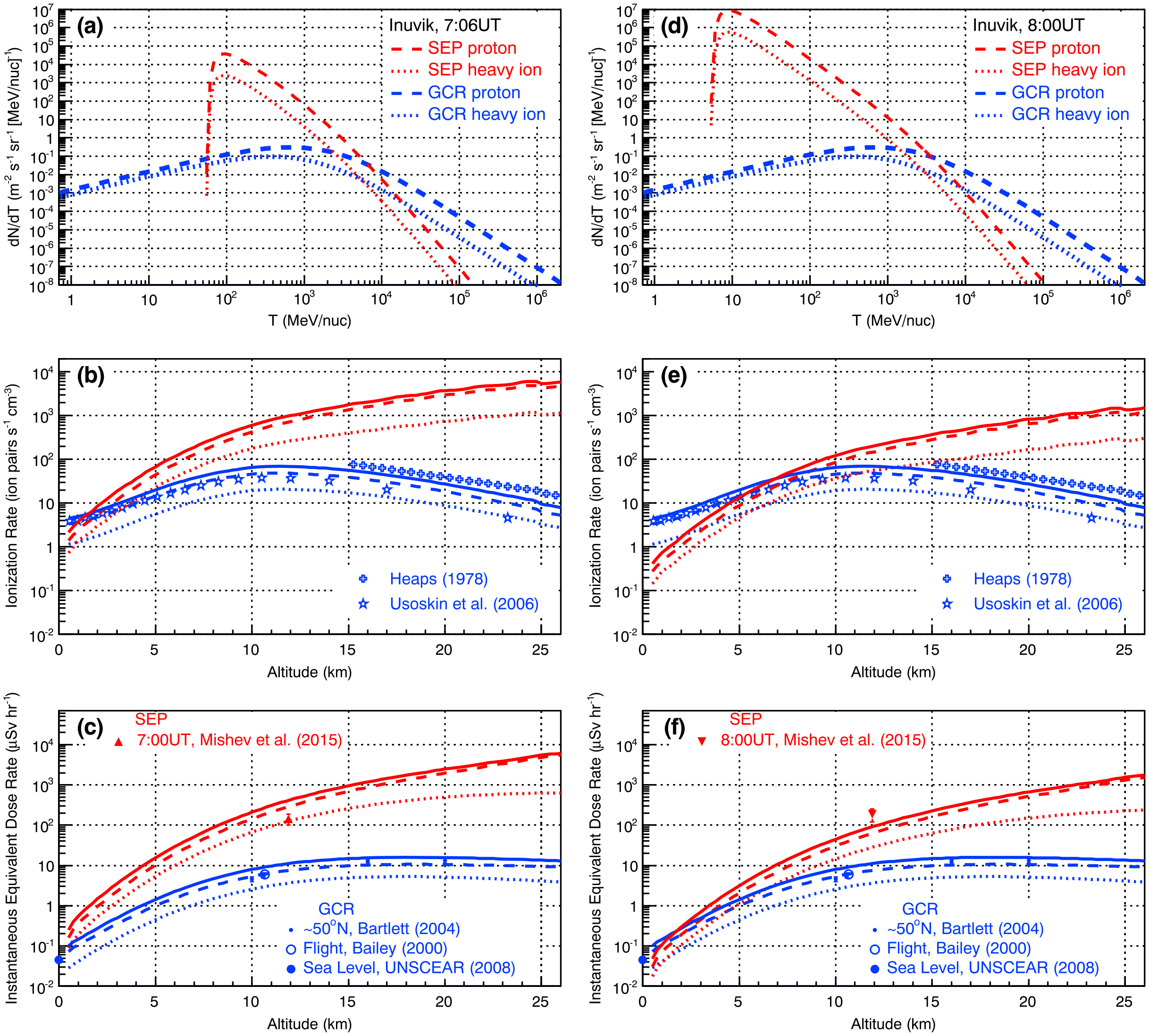

Figure 3. Same as Figure 2 but for the Inuvik (Canada) NM station. Fortunately for air travelers, the relativistic solar particle fluxes were much lower in the north polar region, where commercial air flights are more frequent, compared with the south polar region. An animation of these graphs as a function of time throughout the event is included in the supporting information.

of magnitude. During the decay phase of the GLE, the ionization rate from SEPs is roughly a factor of 3 higher than that from GCRs at both McMurdo and Inuvik.

Near the peak time of this GLE, at sea level, the ionization rate from SEPs was about a factor of 2 over that from GCRs at McMurdo, while the ionization rate from SEPs at Inuvik was only ~25% of that from GCRs. During the decay phase of the GLE, the ionization rate from SEPs was negligible at both locations near the ground. At above ~10 km, ionization rates from SEPs are higher than those from GCRs for all times between 6:50 and 8:00 UT considered at both locations. This is because most charged SEPs have lower energies than most GCRs, and they cannot penetrate the atmosphere to low altitudes, tending to ionize the air only at higher altitudes.

Before comparing with some previous results, we note some potential sources of uncertainty. *Mishev and Velinov* [2014] report very good agreement between data from balloon-borne measurements and FLUKA simulation results for GCR-induced ionization. Nevertheless, this does not guarantee such accuracy for SEP-induced ionization. Their study reveals an effect of the choice of the hadron interaction generator on the order of 15% for GCR-induced ionization. A similar spread among the GCR-induced radiation dose rates from different models was reported by *Bütikofer et al.* [2009]; however, they found a much wider variation of up to 48% among estimates for SEP-induced radiation, when changing only the interaction model. Such an effect of the hadronic interaction generator may be the largest source of uncertainty in our results. As noted earlier, the conversion from NM observations to the time-dependent SEP amplitude requires the use of yield functions, and we estimate that to cause an uncertainty of ~35% in our results. In section 2.2, we noted that our estimated 20% uncertainty in the SEP heavy/*p* ratio should lead to only a 5% uncertainty in the results. Combining these uncertainties in quadrature, we estimate a total uncertainty of ~60% in our results.

We now compare our simulation results for the atmospheric ionization to those from previous analyses. The parameterization of GCR-induced ion-pair production rates from balloon measurements at solar maximum by *Heaps* [1978] and calculations using the CR-induced ionization model by *Usoskin and Kovaltsov* [2006] with our GCR *p* and He spectra are shown by cross and star symbols, respectively, in Figures 2b and 2e and 3b and 3e. Our simulated ionization rate due to GCRs has a profile shape that is consistent with results from both analyses. The magnitude is lower than that of *Heaps* [1978] by ≈20% at above 15 km and greater than that of *Usoskin and Kovaltsov* [2006] by ≈10% at a few kilometers above the ground. These small differences are not unreasonable since there are many caveats in the comparison, such as differences in geomagnetic location, solar modulation, and atmospheric properties. Furthermore, our calculations and the simulated ionization yield functions by *Usoskin and Kovaltsov* [2006] consider only GCRs and neglect other ionization sources such as ultraviolet radiation from the Sun, which may be important at above ~20 km [see *Calisto et al.*, 2011, Figure 1]. This could partly explain the discrepancies with the empirical data based on observations of all ionization sources by *Heaps* [1978]; the present calculations for GCRs are closer to results by *Heaps* [1978] than are the calculations by *Usoskin and Kovaltsov* [2006]. Our simulated ion pair production rates are also qualitatively consistent with other previous studies [see, e.g., *Bazilevskaya et al.*, 2008, Figure 2; *Mishev et al.*, 2012].

Our calculated instantaneous equivalent dose rates at different altitudes are shown in Figures 2c and 2f and 3c and 3f, in which the measured average GCR-generated dose rate received by air crews at typical airplane altitude [*Bailey*, 2000; *Bartlett*, 2004] and at sea level is also shown for comparison. Our simulation results are somewhat higher than the measurements, with improved agreement at higher altitude. The triangles represent calculations of the combined GCR and SEP contribution on 20 January 2005 from *Mishev et al.* [2015] for the north and south polar regions: The upward triangle is for the time at 7:00 UT, and the downward triangle is for 8:00 UT. Comparisons with *Mishev et al.* [2015] are more clearly illustrated in Figure 4. Results from our simulations in Figures 2c and 3c suggest that during the peak of this GLE at ~12 km altitude, the instantaneous radiation dose rate increased by a factor of ~300 above the average GCR rate at McMurdo and by a factor of ~40 at Inuvik.

Time variations of our total (GCR + SEP) ionization and equivalent dose rates at 11.7 km altitude, the value considered by *Mishev et al.* [2015], are shown in Figures 4a and b4. Our simulated equivalent dose rates at McMurdo and Inuvik are consistent with the results by *Mishev et al.* [2015] at 7:00 UT and 8:00 UT at the same altitude as shown in Figure 4b and are qualitatively consistent with Figure 4 in *Bütikofer et al.* [2009].

The world average annual background radiation exposure for humans is ~2.4 mSv, in which ~0.4 mSv is from CRs [*United Nations Scientific Committee on the Effects of Atomic Radiation*, 2008]. The suggested annual limit of radiation exposure for the public is 1 mSv above the background, though a higher dose could be allowed if the 5 year average dose does not exceed 1 mSv/yr [*ICRP*, 2007]. From Movies S1d and S2d in the supporting information, we estimate that an airplane passenger spending ~1 h at 12 km altitude above McMurdo or Inuvik during this GLE would have received ≈0.5 mSv or ≈0.2 mSv additional radiation exposure, respectively, due to the SEPs. Since the NM count rate at Terre Adélie is ≈1.5 times of that at McMurdo (see Figure 1), the most extreme additional radiation dose due to this GLE event could be at least ≈0.75 mSv. These amounts are similar to the average dosage from GCRs during an entire year at ground level and are still within the suggested annual limit of 1 mSv above the background.

For the strongest GLE ever recorded in February 1956, the maximum percent increase of the atmospheric neutron count rate is estimated to be ~9000% near the polar regions [*Duggal*, 1979; *Bieber et al.*, 2013], which is ~4 times the maximum count rate at McMurdo during the January 2005 event and lasted for about 5 h. If we assume that the time profiles of the percent increase for both events near the peak time are similar, a simple scaling of our results would place the radiation dosage received by airplane passengers near the poles during this enormous February 1956 event at around a few millisievert per hour. Passengers spending ~5 h near the polar regions could have been exposed to a dosage which greatly exceeded the suggested annual limit just from this event alone. Even if the accumulated radiation exposure at airplane altitude for either the

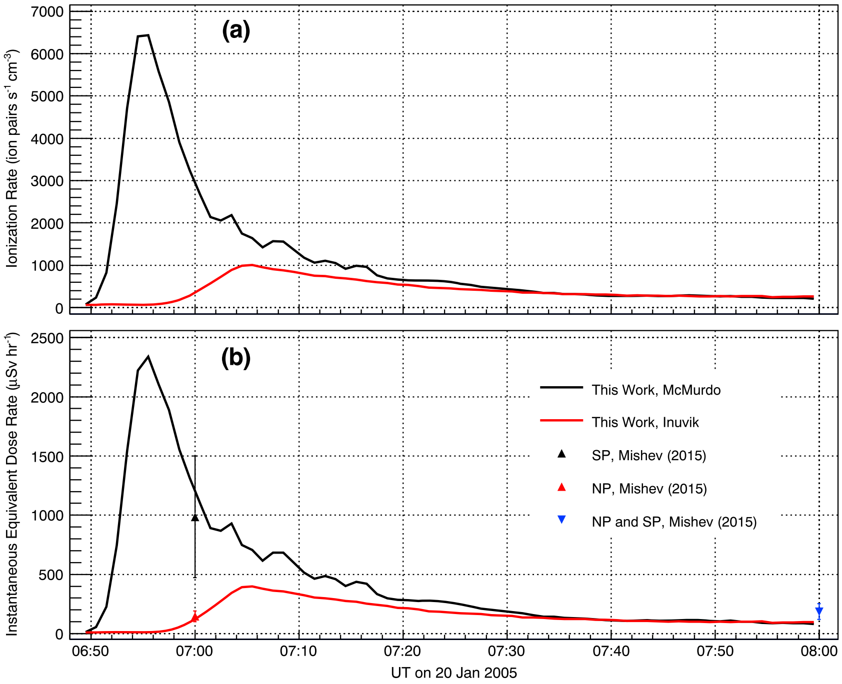

Figure 4. (a) Simulated total (GCR + SEP) ionization and (b) equivalent dose rates in 1 min time steps at 11.7 km above sea level. Results by *Mishev et al.* [2015] at the same altitude for south polar (SP) and north polar (NP) regions are shown for comparison.

2005 or 1956 GLE event does not exceed the suggested annual or 5 year average limit, receiving an enormous amount of radiation in a very short period of time may pose dangerous health effects, which need to be further studied.

Acknowledgments
This research project is supported by Mahidol University, the Thailand Research Fund (grants TRG5880173, BRG5580001, BRG5880009, and RTA5980003 and Royal Golden Jubilee fellowship PHD/0136/2552) and the National Astronomical Research Institute of Thailand (NARIT). P.-S.M. was partially supported under the postdoctoral research sponsorship of Mahidol University. We thank John Bieber for useful discussions, Andrew Snodin for his assistance with cluster computing, and Waraporn Nuntiyakul for providing valuable latitude survey data. For data from the McMurdo and Inuvik neutron monitors, we thank the Bartol Research Institute neutron monitor program, which is supported by the U.S. National Science Foundation via awards PLR-1341562 and PLR-1245939 and their predecessors. The data displayed in the figures are available upon request from the corresponding author.

References

Bailey, S. (2000), Air crew radiation exposure—An overview, *Nuclear News*, *32*, 32–40.

Bartlett, D. T. (2004), Radiation protection aspects of the cosmic radiation exposure of aircraft crew, *Radiat. Prot. Dosim.*, *109*(4), 349–355.

Bazilevskaya, G. A., et al. (2008), Cosmic ray induced ion production in the atmosphere, *Space Sci. Rev.*, *137*, 149–173, doi:10.1007/s11214-008-9339-y.

Bieber, J. W., and P. Evenson (1991), Determination of energy spectra for the large solar particle events of 1989, in *Proceedings of the 22nd International Cosmic Ray Conference*, vol. 3, pp. 129–132, The Inst. for Adv. Studies, Dublin.

Bieber, J. W., et al. (2002), Energetic particle observations during the 2000 July 14 solar event, *Astrophys. J.*, *567*, 622–634.

Bieber, J. W., J. Clem, P. Evenson, R. Pyle, A. Sáiz, and D. Ruffolo (2013), Giant ground level enhancement of relativistic solar protons on 2005 January 20. I. Spaceship Earth observations, *Astrophys. J.*, *771*, 92, doi:10.1088/0004-637X/771/2/92.

Böhlen, T. T., et al. (2014), The FLUKA code: Developments and challenges for high energy and medical applications, *Nuclear Data Sheets*, *120*, 211–214.

Bütikofer, R., E. O. Flückiger, B. Pirard, and L. Desorgher (2009), Effective radiation dose for selected intercontinental flights during the GLEs on 20 January 2005 and 13 December 2006, in *Proc. 21st European Cosmic Ray Symposium*, pp. 158–163, Inst. Exp. Phys. Slovak Acad. Sci., Košice, Slovakia.

Bütikofer, R., and E. O. Flückiger (2011), Radiation doses along selected flight profiles during two extreme solar cosmic ray events, *Astrophys. Space Sci. Trans.*, *7*, 105–109, doi:10.5194/astra-7-105-2011.

Caballero-Lopez, R. A., and H. Moraal (2012), Cosmic-ray yield and response functions in the atmosphere, *J. Geophys. Res.*, *117*, A12103, doi:10.1029/2012JA017794.

Calisto, M., I. Usoskin, E. Rozanov, and T. Peter (2011), Influence of Galactic Cosmic Rays on atmospheric composition and dynamics, *Atmos. Chem. Phys.*, *11*, 4547–4556, doi:10.5194/acp-11-4547-2011.

Cramp, J., et al. (1997), The October 22, 1989, solar cosmic ray enhancement: An analysis of the anisotropy and spectral characteristics, *J. Geophys. Res.*, *102*, 24,237–24,248, doi:10.1029/97JA01947.

Dorman, L. I. (1963), Geophysical and astrophysical aspects of cosmic rays, in *Progress in Elementary Particle and Cosmic Ray Physics*, vol. 7, edited by J. G. Wilson and S. A. Wouthuysen, pp. 1–324, North-Holland, Amsterdam.

Dorman, L. I. (2004), *Cosmic Rays in the Earth's Atmosphere and Underground*, Kluwer, Dordrecht, Netherlands.

Duggal, S. P. (1979), Relativistic solar cosmic rays, *Rev. Geophys.*, *17*(5), 1021–1058.

Ferrari, A., P. R. Sala, A. Fassò, and J. Ranft, (2005), FLUKA: A multi-particle transport code, *Tech. Rep. CERN-2005-10, INFN/TC_05/11, SLAC-R-773*, European Organization for Nuclear Research, Geneva, Switzerland.

Forbush, S. E. (1946), Three unusual cosmic-ray increases possibly due to charged particles from the Sun, *Phys. Rev.*, *70*, 771–772.

Heaps, M. G. (1978), Parametrization of the cosmic ray ion-pair production rate above 18 km, *Planet. Space Sci.*, *26*, 513–517.

ICRP (1996), *Conversion Coefficients for Use in Radiological Protection Against External Radiation*, ICRP Publ. 74, *Ann. ICRP, 26*(3-4).

ICRP (2007), *The 2007 Recommendations of the International Commission on Radiological Protection*, ICRP Publ. 103, *Ann. ICRP, 37*(2-4).

Lin, Z., J. W. Bieber, and P. Evenson (1995), Electron trajectories in a model magnetosphere: Simulation and observation under active conditions, *J. Geophys. Res.*, *100*(A12), 23,543–23,549, doi:10.1029/95JA02696.

Mangeard, P.-S., D. Ruffolo, A. Sáiz, S. Madlee, and T. Nutaro (2016a), Monte Carlo simulation of the neutron monitor yield function, *J. Geophys. Res. Space Physics*, *121*, 7435–7448, doi:10.1002/2016JA022638.

Mangeard, P.-S., et al. (2016b), Dependence of the neutron monitor count rate and time delay distribution on the rigidity spectrum of primary cosmic rays, *J. Geophys. Res. Space Physics*, *121*, 620–636, doi:10.1002/2016JA023515.

Matthiä, D., et al. (2009), Temporal and spatial evolution of the solar energetic particle event on 20 January 2005 and resulting radiation doses in aviation, *J. Geophys. Res.*, *114*, A08104, doi:10.1029/2009JA014125.

Maurin, D., A. Cheminet, L. Derome, A. Ghelfi, and G. Hubert (2015), Neutron monitors and muon detectors for solar modulation studies: Interstellar flux, yield function, and assessment of critical parameters in count rate calculations, *Adv. Space Res.*, *55*, 363–389.

Mewaldt, R. A., et al. (2005), Proton, helium, and electron spectra during the large solar particle events of October–November 2003, *J. Geophys. Res.*, *110*, A09S18, doi:10.1029/2005JA011038.

Mewaldt, R. A. (2006), Solar energetic particle composition, energy spectra, and space weather, *Space Sci. Rev.*, *124*, 303–316.

Mironova, I. A., I. G. Usoskin, G. A. Kovaltsov, and S. V. Petelina (2012), Possible effect of extreme solar energetic particle event of 20 January 2005 on polar stratospheric aerosols: Direct observational evidence, *Atmos. Chem. Phys.*, *12*, 769–778.

Mishev, A. L. (2014), Computation of radiation environment during ground level enhancements 65, 69 and 70 at equatorial region and flight altitudes, *Adv. Space Res.*, *54*, 528–535.

Mishev, A. L., and P. I. Y. Velinov (2014), Influence of hadron and atmospheric models on computation of cosmic ray ionization in the atmosphere—Extension to heavy nuclei, *J. Atmos. Sol. Terr. Phys.*, *120*, 111–120.

Mishev, A. L., P. I. Y. Velinov, L. Mateev, and Y. Tassev (2012), Ionization effect of nuclei with solar and galactic origin in the Earth atmosphere during GLE 69 on 20 January 2005, *J. Atmos. Sol. Terr. Phys.*, *89*, 1–7.

Mishev, A. L., F. Adibpour, I. G. Usoskin, and E. Felsberger (2015), Computation of dose rate at flight altitudes during ground level enhancements no. 69, 70 and 71, *Adv. Space Res.*, *55*, 354–362.

Nuntiyakul, W., et al. (2014), Latitude survey investigation of Galactic cosmic ray solar modulation during 1994–2007, *Astrophys. J.*, *795*, 11, doi:10.1088/0004-637X/795/1/11.

Picone, J. M., A. E. Hedin, D. P. Drob, and A. C. Aikin (2002), NRLMSISE-00 empirical model of the atmosphere: Statistical comparisons and scientific issues, *J. Geophys. Res.*, *107*(A12), 1468, doi:10.1029/2002JA009430.

Porter, H. S., C. H. Jackman, and A. E. S. Green (1976), Efficiencies for production of atomic nitrogen and oxygen by relativistic proton impact in air, *J. Chem. Phys.*, *65*(1), 154, doi:10.1063/1.432812.

Ruffolo, D., et al. (2006), Relativistic solar protons on 1989 October 22: Injection and transport along both legs of a closed interplanetary magnetic loop, *Astrophys. J.*, *639*, 1186–1205.

Sáiz, A., D. Ruffolo, J. W. Bieber, P. Evenson, and R. Pyle (2008), Anisotropy signatures of solar energetic particle transport in a closed interplanetary magnetic loop, *Astrophys. J.*, *672*, 650–658.

United Nations Scientific Committee on the Effects of Atomic Radiation (2008), *Sources and Effects of Ionizing Radiation*, vol. 4, United Nations, New York.

Usoskin, I. G., and G. A. Kovaltsov (2006), Cosmic ray induced ionization in the atmosphere: Full modeling and practical applications, *J. Geophys. Res.*, *111*, D21206, doi:10.1029/2006JD007150.

Usoskin, I. G., G. A. Bazilevskaya, and G. A. Kovaltsov (2011a), Solar modulation parameter for cosmic rays since 1936 reconstructed from ground-based neutron monitors and ionization, *J. Geophys. Res.*, *116*, A02104, doi:10.1029/2010JA016105.

Usoskin, I. G., G. A. Kovaltsov, I. A. Mironova, A. J. Tylka, and W. F. Dietrich (2011b), Ionization effect of solar particle GLE events in low and middle atmosphere, *Atmos. Chem. Phys.*, *11*, 1979–1988.

von Savigny, C., M. Sinnhuber, H. Bovensmann, J. P. Burrows, M.-B. Kallenrode, and M. Schwartz (2007), On the disappearance of noctilucent clouds during the January 2005 solar proton events, *Geophys. Res. Lett.*, *34*, L02805, doi:10.1029/2006GL028106.

PHYSICAL REVIEW D **95,** 082007 (2017)

Cosmic-ray electron-positron spectrum from 7 GeV to 2 TeV with the Fermi Large Area Telescope

S. Abdollahi,[1] M. Ackermann,[2] M. Ajello,[3] W. B. Atwood,[4] L. Baldini,[5] G. Barbiellini,[6,7] D. Bastieri,[8,9] R. Bellazzini,[10] E. D. Bloom,[11] R. Bonino,[12,13,*] T. J. Brandt,[14] J. Bregeon,[15] P. Bruel,[16,†] R. Buehler,[2] R. A. Cameron,[17] R. Caputo,[4] M. Caragiulo,[18,19] D. Castro,[14] E. Cavazzuti,[20] C. Cecchi,[21,22] A. Chekhtman,[23] S. Ciprini,[20,21] J. Cohen-Tanugi,[15] F. Costanza,[19] A. Cuoco,[24,12] S. Cutini,[20,21] F. D'Ammando,[25,26] F. de Palma,[19,27] R. Desiante,[12,28] S. W. Digel,[17] N. Di Lalla,[10] M. Di Mauro,[17] L. Di Venere,[18,19] P. S. Drell,[17] A. Drlica-Wagner,[29] C. Favuzzi,[18,19] W. B. Focke,[17] S. Funk,[30] P. Fusco,[18,19] F. Gargano,[19] D. Gasparrini,[20,21] N. Giglietto,[18,19] F. Giordano,[18,19] M. Giroletti,[25] D. Green,[31,14] L. Guillemot,[32,33] S. Guiriec,[14,34] A. K. Harding,[14] T. Jogler,[35] G. Jóhannesson,[36] T. Kamae,[37] M. Kuss,[10] G. La Mura,[38] L. Latronico,[12] F. Longo,[6,7] F. Loparco,[18,19] P. Lubrano,[21] S. Maldera,[12] D. Malyshev,[30] A. Manfreda,[5,‡] M. N. Mazziotta,[19] P. F. Michelson,[17] N. Mirabal,[14,34] W. Mitthumsiri,[39] T. Mizuno,[40] A. A. Moiseev,[41,31] M. E. Monzani,[17] A. Morselli,[42] I. V. Moskalenko,[17] M. Negro,[12,13] E. Nuss,[15] E. Orlando,[17] D. Paneque,[43] J. S. Perkins,[14] M. Pesce-Rollins,[10] F. Piron,[15] G. Pivato,[10] T. A. Porter,[17] G. Principe,[30] S. Rainò,[18,19] R. Rando,[8,38] M. Razzano,[10,44] A. Reimer,[45,17] O. Reimer,[45,17] C. Sgrò,[10] D. Simone,[19] E. J. Siskind,[46] F. Spada,[10] G. Spandre,[10] P. Spinelli,[18,19] H. Tajima,[47,17] J. B. Thayer,[17] L. Tibaldo,[48] D. F. Torres,[49,50] E. Troja,[14,31] M. Wood,[17] A. Worley,[51] G. Zaharijas,[52,53] and S. Zimmer[54]

(The Fermi-LAT Collaboration)

[1]*Department of Physical Sciences, Hiroshima University, Higashi-Hiroshima, Hiroshima 739-8526, Japan*

[2]*Deutsches Elektronen Synchrotron DESY, D-15738 Zeuthen, Germany*

[3]*Department of Physics and Astronomy, Clemson University, Kinard Lab of Physics, Clemson, South Carolina 29634-0978, USA*

[4]*Santa Cruz Institute for Particle Physics, Department of Physics and Department of Astronomy and Astrophysics, University of California at Santa Cruz, Santa Cruz, California 95064, USA*

[5]*Università di Pisa and Istituto Nazionale di Fisica Nucleare, Sezione di Pisa I-56127 Pisa, Italy*

[6]*Istituto Nazionale di Fisica Nucleare, Sezione di Trieste, I-34127 Trieste, Italy*

[7]*Dipartimento di Fisica, Università di Trieste, I-34127 Trieste, Italy*

[8]*Istituto Nazionale di Fisica Nucleare, Sezione di Padova, I-35131 Padova, Italy*

[9]*Dipartimento di Fisica e Astronomia "G. Galilei," Università di Padova, I-35131 Padova, Italy*

[10]*Istituto Nazionale di Fisica Nucleare, Sezione di Pisa, I-56127 Pisa, Italy*

[11]*W. W. Hansen Experimental Physics Laboratory, Kavli Institute for Particle Astrophysics and Cosmology, Department of Physics and SLAC National Accelerator Laboratory, Stanford University, Stanford, California 94305, USA*

[12]*Istituto Nazionale di Fisica Nucleare, Sezione di Torino, I-10125 Torino, Italy*

[13]*Dipartimento di Fisica, Università degli Studi di Torino, I-10125 Torino, Italy*

[14]*NASA Goddard Space Flight Center, Greenbelt, Maryland 20771, USA*

[15]*Laboratoire Univers et Particules de Montpellier, Université Montpellier, CNRS/IN2P3, F-34095 Montpellier, France*

[16]*Laboratoire Leprince-Ringuet, École polytechnique, CNRS/IN2P3, F-91128 Palaiseau, France*

[17]*W. W. Hansen Experimental Physics Laboratory, Kavli Institute for Particle Astrophysics and Cosmology, Department of Physics and SLAC National Accelerator Laboratory, Stanford University, Stanford, California 94305, USA*

[18]*Dipartimento di Fisica "M. Merlin" dell'Università e del Politecnico di Bari, I-70126 Bari, Italy*

[19]*Istituto Nazionale di Fisica Nucleare, Sezione di Bari, I-70126 Bari, Italy*

[20]*Agenzia Spaziale Italiana (ASI) Science Data Center, I-00133 Roma, Italy*

[21]*Istituto Nazionale di Fisica Nucleare, Sezione di Perugia, I-06123 Perugia, Italy*

[22]*Dipartimento di Fisica, Università degli Studi di Perugia, I-06123 Perugia, Italy*

[23]*College of Science, George Mason University, Fairfax, VA 22030, resident at Naval Research Laboratory, Washington, District of Columbia 20375, USA*

[24]*RWTH Aachen University, Institute for Theoretical Particle Physics and Cosmology, (TTK), D-52056 Aachen, Germany*

[25]*INAF Istituto di Radioastronomia, I-40129 Bologna, Italy*

[26]*Dipartimento di Astronomia, Università di Bologna, I-40127 Bologna, Italy*

[27]*Università Telematica Pegaso, Piazza Trieste e Trento, 48, I-80132 Napoli, Italy*

[28]*Università di Udine, I-33100 Udine, Italy*

[29]*Center for Particle Astrophysics, Fermi National Accelerator Laboratory, Batavia, Illinois 60510, USA*

[30]*Erlangen Centre for Astroparticle Physics, D-91058 Erlangen, Germany*

[31]*Department of Physics and Department of Astronomy, University of Maryland, College Park, Maryland 20742, USA*
[32]*Laboratoire de Physique et Chimie de l'Environnement et de l'Espace - Université d'Orléans / CNRS, F-45071 Orléans Cedex 02, France*
[33]*Station de radioastronomie de Nançay, Observatoire de Paris, CNRS/INSU, F-18330 Nançay, France*
[34]*NASA Postdoctoral Program Fellow, USA*
[35]*Friedrich-Alexander-Universität, Erlangen-Nürnberg, Schlossplatz 4, 91054 Erlangen, Germany*
[36]*Science Institute, University of Iceland, IS-107 Reykjavik, Iceland*
[37]*Department of Physics, Graduate School of Science, University of Tokyo, 7-3-1 Hongo, Bunkyo-ku, Tokyo 113-0033, Japan*
[38]*Dipartimento di Fisica e Astronomia "G. Galilei", Università di Padova, I-35131 Padova, Italy*
[39]*Department of Physics, Faculty of Science, Mahidol University, Bangkok 10400, Thailand*
[40]*Hiroshima Astrophysical Science Center, Hiroshima University, Higashi-Hiroshima, Hiroshima 739-8526, Japan*
[41]*Center for Research and Exploration in Space Science and Technology (CRESST) and NASA Goddard Space Flight Center, Greenbelt, Maryland 20771, USA*
[42]*Istituto Nazionale di Fisica Nucleare, Sezione di Roma "Tor Vergata," I-00133 Roma, Italy*
[43]*Max-Planck-Institut für Physik, D-80805 München, Germany*
[44]*Funded by contract FIRB-2012-RBFR12PM1F from the Italian Ministry of Education, University and Research (MIUR)*
[45]*Institut für Astro- und Teilchenphysik and Institut für Theoretische Physik, Leopold-Franzens-Universität Innsbruck, A-6020 Innsbruck, Austria*
[46]*NYCB Real-Time Computing Inc., Lattingtown, New York 11560-1025, USA*
[47]*Solar-Terrestrial Environment Laboratory, Nagoya University, Nagoya 464-8601, Japan*
[48]*Max-Planck-Institut für Kernphysik, D-69029 Heidelberg, Germany*
[49]*Institute of Space Sciences (IEEC-CSIC), Campus UAB, E-08193 Barcelona, Spain*
[50]*Institució Catalana de Recerca i Estudis Avançats (ICREA), Barcelona E-08010, Spain*
[51]*Department of Physics and Astronomy, University of Denver, Denver, Colorado 80208, USA*
[52]*Istituto Nazionale di Fisica Nucleare, Sezione di Trieste, and Università di Trieste, I-34127 Trieste, Italy*
[53]*Laboratory for Astroparticle Physics, University of Nova Gorica, Vipavska 13, SI-5000 Nova Gorica, Slovenia*
[54]*University of Geneva, Department of Nuclear and Particle Physics, 24 quai Ernest-Ansermet, CH-1211 Geneva 4, Switzerland*

(Received 21 September 2016; revised manuscript received 28 March 2017; published 21 April 2017)

We present a measurement of the cosmic-ray electron + positron spectrum between 7 GeV and 2 TeV performed with almost seven years of data collected with the *Fermi* Large Area Telescope. We find that the spectrum is well fit by a broken power law with a break energy at about 50 GeV. Above 50 GeV, the spectrum is well described by a single power law with a spectral index of 3.07 ± 0.02 $(\mathrm{stat} + \mathrm{syst}) \pm 0.04(\mathrm{energy\ measurement})$. An exponential cutoff lower than 1.8 TeV is excluded at 95% CL.

DOI: 10.1103/PhysRevD.95.082007

I. INTRODUCTION

While propagating throughout the Galaxy, high-energy cosmic-ray electrons and positrons (CRE) rapidly lose energy by interacting with the interstellar radiation field through inverse Compton scattering and by synchrotron emission on the Galactic magnetic field. Their diffusion distance is several hundred parsecs at 1 TeV, much shorter than the radial scale of the Galaxy [1]. Therefore, the shape of the CRE spectrum from ∼100 GeV up to several TeV (as well as the positron fraction [2–4] and CRE anisotropy [5]) can provide evidence for local CRE sources of astrophysical (supernova remnants and pulsar wind nebulae [6–11]) or exotic (dark matter [12–14]) nature.

Recent measurements by AMS-02 [15] and *Fermi* [16] have shown that the CRE spectrum can be fit with a single power law up to ∼1 TeV, with an index of 3.170 ± 0.008 and 3.08 ± 0.05, respectively. The H.E.S.S. [17,18] measurements gave the first indication of a cutoff at ∼2 TeV. These results can be interpreted as local CRE sources with a spectral cutoff at about this energy [19].

The *Fermi* Large Area Telescope (LAT) [20], while designed to detect gamma rays, is able to collect and identify CREs with a large acceptance by combining

---

[*] rbonino@to.infn.it
[†] Philippe.Bruel@llr.in2p3.fr
[‡] alberto.manfreda@pi.infn.it

information from its three subsystems, a silicon-strip detector based tracker-converter (TKR), an imaging calorimeter (CAL) consisting of eight layers of CsI crystals and an anticoincidence detector (ACD) constructed from tiles of plastic scintillator surrounding the TKR and CAL.

Extending the CRE energy measurement beyond 1 TeV with the LAT is challenging because, at such high energy, only ~35% of the shower is on average contained in the CAL and a significant fraction of the CAL crystals along the shower axis are saturated (crystal saturation occurs when more than ~70 GeV is deposited in one crystal, which occurs for CREs above ~600 GeV). Thanks to the new Pass 8 event analysis [21], with improved track and shower reconstruction as well as improved multivariate methods for background suppression, we can achieve a level of background contamination smaller than 25% and an energy resolution (defined as the half-width of the 68% containment range) better than 20% up to 2 TeV.

In this article, we present an updated measurement of the CRE spectrum, using almost seven years of LAT Pass 8 data up to 2 TeV, performing the first direct measurement above 1 TeV. A search for anisotropies, using the same data and event selection, and a theoretical interpretation of the CRE spectrum are presented in separate publications [22] [23].

The paper is structured as follows: the event selection is introduced in Sec. II and further detailed in the two following sections. The energy measurement and the study of systematic uncertainties are described in Secs. V and VI, respectively, while the results are presented and discussed in Sec. VII.

II. EVENT SELECTION

The LAT on-board gamma filter is designed to reject charged particles, but it accepts all events with a deposited energy in the CAL larger than 20 GeV. As in the previous LAT CRE measurement [16], we performed two independent analyses: the high-energy (HE) analysis above 42 GeV and the low-energy (LE) analysis between 7 and 70 GeV. The former selects events passing the on-board gamma filter, whereas for the latter we use an unbiased sample of all trigger types, prescaled on-board by a factor of 250. In both analyses, we first apply a set of simple cuts before performing a multivariate analysis in order to reduce as much as possible the residual proton contamination.

We use LAT Pass 8 data collected between August 4, 2008, and June 24, 2015, requiring that the rocking angle of the LAT from the zenith is less than 51 degrees. The overall live time for this data set is 4.68 years. We select events within 60 degrees from the LAT boresight in order to eliminate potential contamination from photons produced in cosmic-ray induced air showers in Earth's atmosphere. The so-called photon Earth limb is located at 113 degrees from the zenith.

We require events with a well reconstructed track, whose path lengths through the CAL are larger than 8 radiation lengths. The event energy is estimated by fitting the shower profile in the CAL. We reject badly reconstructed events by requiring that the $\chi^2/\mathrm{n.d.f.}$ of the shower profile fit is less than 20. In order to remove alphas and heavier ions we use the path-length-corrected signal in the ACD and the TKR time over threshold which provide charge-deposition information. Both variables are sensitive to the ionization signal which is proportional to Z^2. Applying a cut in the plane spanned by these two variables around the $Z = 1$ group reduces contamination of alphas and ions to less than a few per mil with respect to protons. This cut also reduces the residual contribution from celestial photons below 1% of the CRE flux. The LE selection requires more than 2 GeV deposited in the CAL.

For both the HE and the LE analyses, these cuts (hereafter referred to as "precuts") are combined with further selections based on multivariate classification analyses. We use the multivariate analysis toolkit TMVA [24] to train boosted decision trees (BDT) with simulated data sets. After training, each BDT provides a variable p_{BDT} between -1 and $+1$, corresponding to most protonlike and most electronlike events, respectively. Since the p_{BDT} distribution for electrons peaks very sharply at 1, we use $P_{\mathrm{CRE}} = \log_{10}(1 - p_{\mathrm{BDT}})$ as the CRE estimator. For each energy bin of the analyses, we fit the distribution of P_{CRE} with two templates corresponding to simulated electrons and background, respectively. After choosing the cut on P_{CRE} that selects the CRE candidates, we use the result of the template fit to estimate and subtract the number of residual background events. The HE and LE multivariate analyses are described in the two following sections.

The simulated data sets that are used to train the BDTs were generated with the standard LAT Monte Carlo (MC) suite [20], a detailed simulation of the passage of particles through the LAT based on the GEANT4 package [25]. Independent simulated data sets were produced to perform data/MC comparisons, model the CRE acceptance and estimate the residual background contamination. Above 42 GeV, the residual background after precuts due to nonproton particles is negligible compared to that due to protons, so the Monte Carlo background sample used in the HE analysis is the output of a pure proton simulation, from 4 GeV to 20 TeV. For the LE analysis, the background MC sample used for the training is a simulation of cosmic rays of both primary and secondary origin in low Earth orbit and Earth limb photons [26].

III. HIGH-ENERGY ANALYSIS

To account for the rapid changes in event topology in the LAT between several GeV and several TeV, we define eight bins in measured energy (equally spaced in $\log_{10} E$ between 31.6 GeV and 3.16 TeV) and train a BDT for each bin. All BDTs are trained with the same set of variables among the hundreds computed during the LAT event reconstruction. These variables were proven to be the most efficient ones in discriminating between electrons and protons thanks to an optimization procedure using only MC data sets.

These discriminating variables characterize the shower trajectory and topology using information from the CAL and TKR subsystems. We use TKR-only information, such as the average time over threshold and the number of hits in the three sections of the TKR, as well as CAL-only information, such as estimates of the shower transverse size, the crystal-based χ^2 of the shower profile fit, and the ratio of the energies deposited in the first and second CAL layers. We also use TKR-CAL information like the ratio of the number of TKR hits to the energy deposited in the first two CAL layers and the distance of closest approach of the CAL cluster centroid to the track.

A. Data/MC agreement

The agreement between data and simulation for P_{CRE} is critical to the analysis: it ensures the goodness of the template fit, from which the background contamination is estimated, and it drives the precision of the selection efficiency predicted by the simulation. As this agreement depends on the data/MC agreement of the individual variables used as input to the BDTs, we performed a systematic comparison of their distributions measured in data and predicted by the simulation for electrons at various energies (eight bins in $\log_{10} E$ between 31.6 GeV and 3.16 TeV) and incidence angles (five bins in $\cos\theta$ between 0.5 and 1, where θ is the angle between the event direction and the LAT boresight).

We found that the widths of the distributions are in good agreement (within 15%), but, for some variables, the position of the peak is shifted. From the differences of peak positions between data and MC, we derived additive corrections that we parametrized as functions of energy and incidence angle, to ensure good data/MC agreement. We refer to these corrections as the individual variables calibration (IVC) corrections. Rather than applying them to the simulation, we apply them to data. Both solutions are equivalent with respect to BDT efficiency (because the IVC corrections are simple shifts) but the latter is more computationally convenient as it does not require retraining the BDTs.

Figure 1 shows the energy dependence of the peak positions for two variables, the transverse size of the shower and the crystal-based χ^2 of the shower profile fit, for data and MC. Although the data/MC discrepancy for the transverse size of the shower could be solved by rescaling the energy, it is not the case for the crystal-based χ^2 of the shower profile fit. As a consequence, these disagreements are not an indication of a problem in energy measurement. We believe that they are the consequence of imperfections in the instrument simulation.

The effect of the IVC corrections is clearly visible in Fig. 2 for the transverse size of the shower, which is one of the variables with the largest data/MC discrepancy. The general trend is that, before correction, the shifts increase with energy and can be as large as the distribution RMS. After correction, the residual differences between peak positions are less than 10% of the distribution RMS; we take them into account when estimating the systematic uncertainties, as described in Sec. VI.

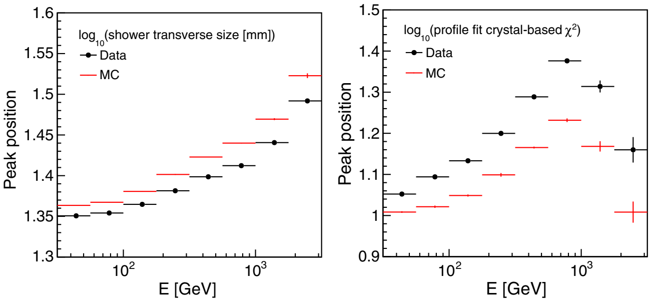

FIG. 1. Energy dependence of the peak position of the distribution of two variables: the logarithm of the transverse size of the shower (left) and the logarithm of the crystal based χ^2 of the shower profile fit (right). The black and red points correspond to data and simulation, respectively.

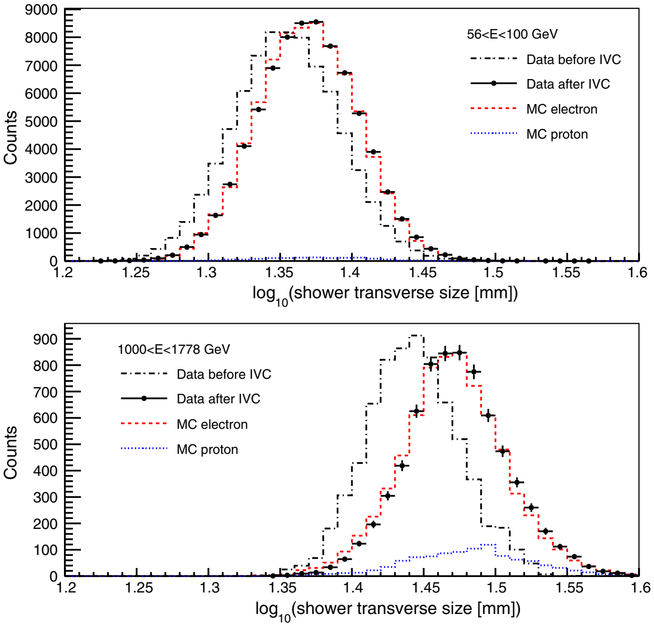

FIG. 2. The logarithm of the shower transverse size before (*black lines*) and after (*black circles*) IVC correction for events between 56 and 100 GeV (top) and between 1 and 1.78 TeV (bottom). The contribution from residual background (blue) has been subtracted from the data distributions. The red histograms correspond to the electron simulation.

B. Template fit

For each energy bin, we construct the MC electron and proton distributions of P_{CRE} and use them as templates: we fit the P_{CRE} distribution of the data with the sum of two MC

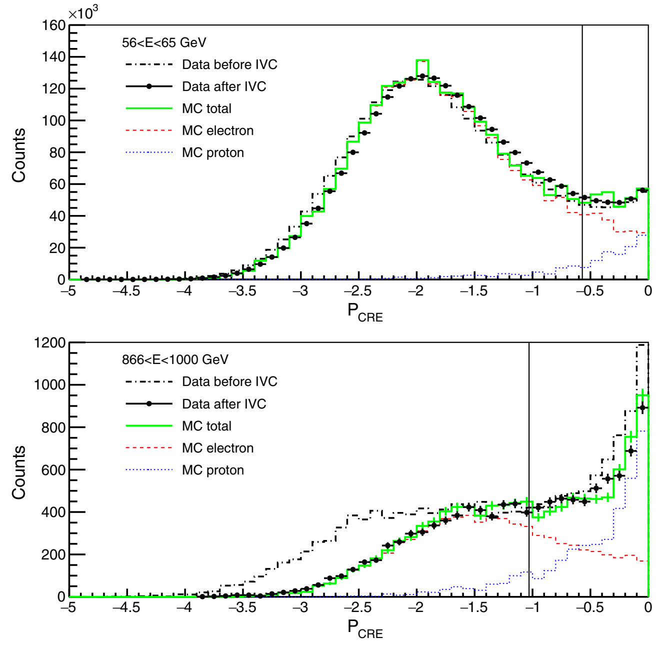

FIG. 3. The result of the template fit in two energy bins [56, 65 GeV] (top) and [866, 1000 GeV] (bottom). For both energy bins, the fit is performed over the interval [−5, 0] and the x-axis range is chosen to focus on the electron peak region. The data P_{CRE} distribution is shown before (black lines) and after (black circles) IVC corrections. The green histograms correspond to the sum of the electron (red) and proton (blue) templates. The vertical line show for each energy bin the position of the selection cut $P_{\mathrm{CRE}} < P_{\mathrm{cut}}$.

templates whose normalizations are the two parameters of the fit.

Ideally, we would perform the fit over the whole range of P_{CRE}. Unfortunately, the data/MC agreement after IVC corrections is not good enough in the "pure" proton range, i.e., for P_{CRE} above ∼0. This is simply due to the fact that the initial data/MC disagreement of individual variables is not always the same for electrons and protons. The IVC corrections, which are optimized for electrons, cannot ensure a good data/MC agreement for protons. As a result, the peak of the proton P_{CRE} distribution ($P_{\mathrm{CRE}} \gtrsim 0$) is not well reproduced by the simulation.

To mitigate the effect of the data/MC discrepancy near the proton peak we restrict the template fit to an interval $P_{\mathrm{CRE}} < P_{\mathrm{max}}$. To find the optimal value of P_{max} we looked at how the χ^2 of the template fit depends on it. We performed a scan starting at $P_{\mathrm{max}} = -1$, which is well outside the proton peak, but still above the predicted position of the maximum of the signal distribution, and then progressively increasing it. We found that the $\chi^2/\mathrm{n.d.f.}$ remains flat until the fit interval starts to comprise a significant part of the proton peak and we chose P_{max} for which the χ^2 has doubled compared to its initial plateau. Because the data/MC disagreement is larger at high energy, the chosen value of P_{max} decreases with energy, as can be seen in Fig. 5.

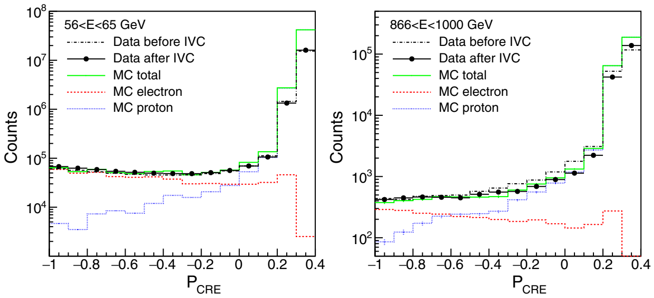

FIG. 4. The result of the template fit in two energy bins [56, 65 GeV] (left) and [866, 1000 GeV] (right). For both energy bins, the fit is performed over the interval [-5,0] and the x-axis range is chosen to focus on the proton peak region. The data P_{CRE} distribution is shown before (black lines) and after (black circles) IVC corrections. The green histograms correspond to the sum of the electron (red) and proton (blue) templates.

Figures 3 and 4 show the result of the template fit in two energy bins. One can see that the IVC corrections improve the data/MC agreement for the electron peak but not for the proton peak.

It is to be noted that the data/MC disagreement for the proton peak of the P_{CRE} distribution is not an issue for the CRE analysis: the residual background contamination corresponds to protons whose showers appear very much like electromagnetic showers. So, by construction, the IVC corrections are valid for these events and we expect the tail of the proton P_{CRE} distribution in the signal region to be well reproduced by the simulation.

C. High-energy selection

We define our selection by looking, in each energy bin, for the cut on P_{CRE} which minimizes the flux uncertainty, taking into account all systematics (discussed in Sec. VI). The minimum is not very pronounced, especially above 100 GeV. We choose to apply a slightly harder cut between 300 GeV and 2 TeV, in order to facilitate the IVC corrections, whose precision benefits from a low residual background contamination. Figure 5 shows the P_{CRE} selection cut and its efficiency as a function of energy.

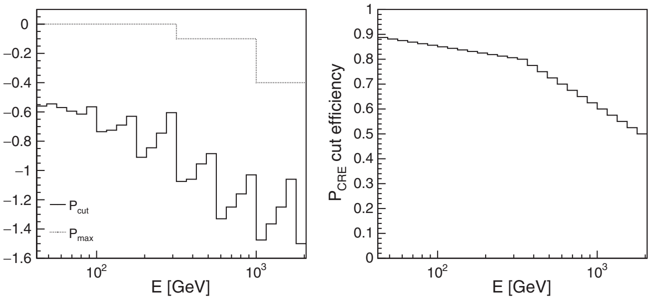

FIG. 5. Left: P_{CRE} selection cut (solid) and P_{max}, the upper end of the template fit interval (dotted), as a function of energy. Right: efficiency of the P_{CRE} selection cut as a function of energy.

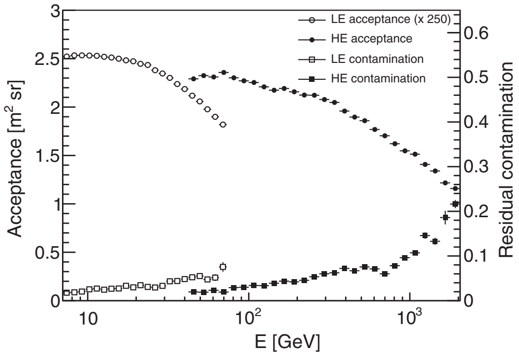

FIG. 6. Acceptance and residual background contamination as a function of energy. The displayed LE acceptance is multiplied by 250 (as if there were no prescale factor due to the on-board filter).

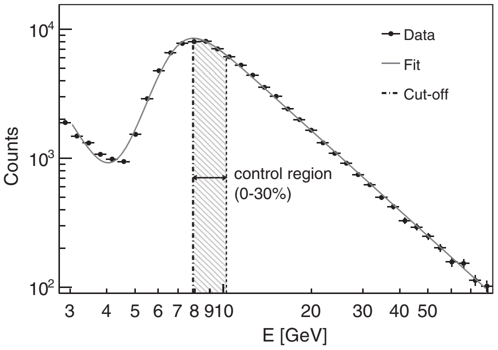

FIG. 7. Fit of the count spectrum for the McIlwain L bin [1.44, 1.49]. The control region, used in the estimation of the systematic uncertainties, corresponds to the interval $[E_c, 1.3E_c]$, where E_c is the measured energy cutoff.

The steps seen every four bins in the selection cut correspond to the transitions between the different P_{CRE} estimators at the boundaries of the BDT $\log_{10} E$ bins. The P_{CRE} selection cut is well below $P_{\max}$.

The acceptance and the residual background contamination (defined as the ratio of the number of residual background events to the total number of events) for the HE selection are shown in Fig. 6. The fact that the acceptance decreases with energy, while the residual contamination increases, highlights the increasing difficulty of the background rejection with energy. Because the IVC corrections procedure requires enough statistics and at the same time a low background contamination, we stop the HE analysis when the residual contamination reaches 20%, which occurs at 2 TeV.

IV. LOW-ENERGY ANALYSIS

The LE selection is based on the same multivariate analysis approach as used for the HE selection. Because the energy range of the LE selection is much smaller than the HE one, we trained only one BDT, with a set of variables optimized for the LE energy range. Since the LE analysis stops at 70 GeV, there is no need to apply the IVC corrections.

The cut on P_{CRE} as a function of energy is set so that the cut efficiency for electrons is ~90% from 7 GeV to 20 GeV and decreases to ~65% at 70 GeV. The residual background contamination is estimated by the same template fitting technique used in the HE analysis. The acceptance and the residual background contamination for the LE selection are shown in Fig. 6.

Below ~20 GeV, the flux of CREs observed by the LAT is strongly influenced by the shielding effect of the magnetic field of the Earth. At a given geomagnetic position and direction with respect to zenith, Galactic charged particles can reach the detector only if they are above a certain rigidity. The dependence of the rigidity cutoff on location can be conveniently parametrized by the McIlwain L parameter [27]. Geographic coordinates with the same McIlwain L parameter are magnetically equivalent from the standpoint of incoming charged particles. The orbit of *Fermi* spans an interval of McIlwain L of 0.98–1.73, corresponding to vertical rigidity cutoff values from ~6 GeV to ~14 GeV. Therefore, measuring the CRE spectrum at a given energy E requires selecting data collected in a McIlwain L interval in which the rigidity cutoff is smaller than E.

In order to parametrize the relation between the rigidity cutoff and McIlwain L, we fit the count spectrum in 15 McIlwain L bins with $f(E) = c_s E^{-\gamma_s} + c_p E^{-\gamma_p}/(1 + (E/E_0)^{-\alpha})$. The first term in $f(E)$ corresponds to secondary CREs while the second term in $f(E)$ corresponds to primary CREs,[1] which are suppressed below the energy E_0. An example of this fit is shown in Fig. 7. We use the position of the maximum of the second term as a measure of the local value of the energy cutoff E_c averaged over the instrument acceptance.

We map the dependence of the energy cutoff on the McIlwain L parameter with the empirical relation $E_c = -14.91 + 67.25/\mathrm{L} - 75.71/\mathrm{L}^2 + 39.44/\mathrm{L}^3$. For each energy bin of the CRE spectrum, we use this relation to find the McIlwain L value $\mathrm{L}_{\min}$ corresponding to the lower boundary of the energy bin and select data collected in regions with $\mathrm{L} > \mathrm{L}_{\min}$. The corresponding fraction of live time spent by the LAT in the selected regions is ~1.25% in the lowest energy bin (from 7 to 7.8 GeV) and becomes ~100% above ~18.2 GeV (see Fig. 8).

Even above the nominal rigidity cutoff a fraction of electrons and positrons is prevented from reaching the detector by the magnetic shadow of the Earth. In order to estimate this fraction of undetected CREs, we use the particle trajectory tracing code (hereafter "tracer") developed by

---

[1] In this section, we refer to primary CREs as electrons of Galactic origin, and to secondary CREs as splash and reentrant electrons produced in the interactions of primaries in the Earth's atmosphere.

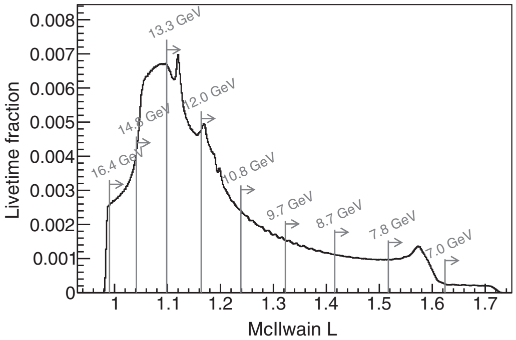

FIG. 8. Normalized distribution of the instrument live time in different McIlwain L bins for the data sample. Grey lines show the McIlwain L cut in each energy bin (with numbers indicating the lower edge of the bin).

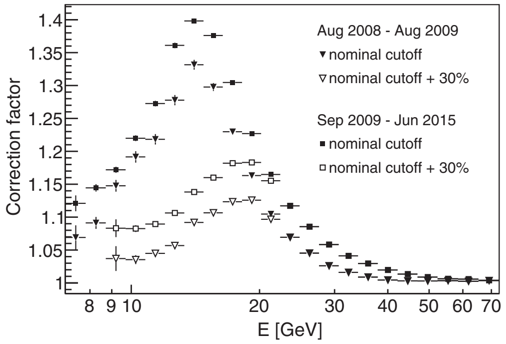

FIG. 9. LE correction factors for the first year of the mission (triangles) and for the following years (squares). Full markers correspond to the nominal energy cutoff, while the empty markers correspond to a cutoff 30% higher. Both are almost identical above 22 GeV.

Smart and Shea [27] and the 2010 model of the Earth's magnetic field from the International Geomagnetic Reference Field (IGRF) [28], as we did in [29]. For efficiency's sake, the tracer computes the trajectories of test particles in the reverse direction, starting from the spacecraft. The test particles (electrons and positrons) are generated according to a power law with an index of 3.2 using the abundance ratios measured by AMS-02 for electrons and positrons [4].

We consider test particles with trajectories reaching 20 Earth radii to have escaped the geomagnetic field, thus corresponding to CREs actually observed by the instrument, while trajectories intersecting the Earth's atmosphere correspond to lost particles. For a given McIlwain L selection, we use the tracer output to estimate the fraction of the latter.

The effect of the geomagnetic field on the loss of primaries is enhanced by a combination of the wide angular aperture of the LAT and its periodic rocking motion with respect to the local zenith, with the result that the edge of the field of view is often very close to the Earth. Because of the rocking angle dependence, we derived correction factors separately for the first year of the mission (rocking angle of 35°) and for the following years (rocking angle of 50°). These correction factors are shown in Fig. 9, as well as the correction factors that we obtain when considering energy cutoffs 30% higher. When estimating the systematic uncertainty for the LE analysis, we vary the energy cutoff choice between E_c and $1.3E_c$. For each energy cutoff, we derive the corresponding McIlwain L selection and tracer correction and compute the CRE flux. The CRE fluxes that we obtain are within 3% of the nominal flux despite the large variation of the tracer correction.

V. ENERGY MEASUREMENT

As for the previous versions of the LAT event analysis Passes 6 and 7, the Pass 8 energy reconstruction above ~5 GeV is performed by fitting the longitudinal shower profile, using the 8 CAL layer energies. The fit parameters are the energy and two parameters that describe the shape of the profile: the shape parameter α and the position of the shower maximum $T_{\max}$. Further details on the profile fit can be found in Appendix A.

Pass 8 improves the energy reconstruction and extends the energy range up to at least 2 TeV. Figure 10 shows that the energy resolution (defined as the half-width of the 68% containment range) ranges from 4% at 10 GeV to 8% at 800 GeV. Above 800 GeV the energy reconstruction is more difficult because of both low shower containment and crystal saturation. As a result the energy resolution increases more rapidly up to 17% at 2 TeV.

Compared to the previous CRE LAT analysis [16], the energy resolution is significantly improved: at 1 TeV the 68% and 95% containment half-widths were 14% and 34%, respectively. With Pass 8 they are 10% and 25%, while the gain in acceptance is 50%.

In order to define a subclass of events with a better energy resolution, which is used in Sec. VII to test the sensitivity of

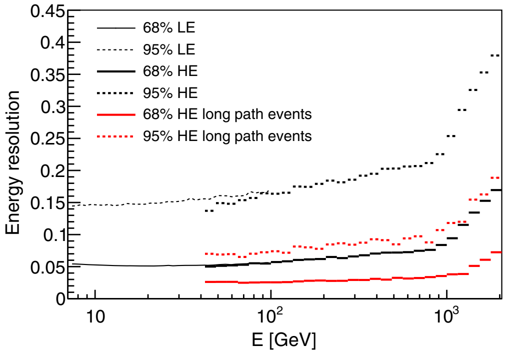

FIG. 10. Energy resolution for various selections: all events (black), events with more than 12 radiation lengths in the CAL (red). Solid (dotted) lines correspond to the 68% (95%) containment halfwidth. Thin and thick lines correspond to the LE and the HE analysis, respectively.

the spectrum to energy resolution, we select events with a CAL path-length greater than 12 X_0. It corresponds to ∼15% of the whole data set. The average CAL path-length of this long-path-events selection is 13.3 X_0 and the energy resolution is 4% at 1 TeV and 8% at 2 TeV.

Because the CAL is only 8.6 X_0 long on-axis, the showers of electrons in the energy range of our analysis are not fully contained. The shower leakage is corrected for by the energy reconstruction. Therefore we have to consider two independent sources of systematic uncertainties for the measured energy. The first one is the uncertainty of the absolute energy scale and the second one is the uncertainty induced by the energy reconstruction. The estimation of these uncertainties is described below.

The geomagnetic cutoff in the CRE spectrum at about 10 GeV provides a spectral feature that allows an absolute calibration of the LAT energy scale. At this energy, the leakage from the CAL is ∼20% and the shower maximum lies in the middle of the CAL. As a consequence, the shower profile fit allows a precise energy reconstruction and the systematic uncertainty on the energy reconstruction at 10 GeV is negligible.

A previous measurement of the geomagnetic cutoff was used to check the LAT energy scale based on one year of LAT data [29]. The same analysis, using almost seven years of Pass 8 data, is reported in Appendix B. We find that the ratio of the measured to expected geomagnetic cutoff is $1.033 \pm 0.004(\mathrm{stat}) \pm 0.020(\mathrm{syst})$. As a result, we decrease the event energies in data by −3.3% in both the LE and HE analyses and conclude that the systematic uncertainty on the absolute energy scale is 2%.

Above 10 GeV the shower leakage increases linearly with $\log_{10} E$ and the shower maximum gets closer to the end of the CAL. Therefore we expect that a potential systematic bias on the energy reconstruction would increase with the energy as well. For each event, the rear leakage corresponds to the extrapolation of the shower profile beyond the total amount of radiation lengths seen by the shower. The precision of this extrapolation depends on the precision we have on the parameters of the fit that drive the shower shape. In order to assess this precision, we compare the distributions of α and T_{max} in data and in the simulation, as shown in Fig. 11 for events between 1 and 1.78 TeV. We find that the data/MC differences as a function of energy for α and T_{max} are, respectively, within $\pm\delta_\alpha(E)$ and $\pm\delta_T(E)$, with $\delta_\alpha(E) = 0.05\log_{10}(E/[10\,\mathrm{GeV}])$ and $\delta_T(E) = 0.1\log_{10}(E/[10\,\mathrm{GeV}])$.

We estimate the uncertainty due to shower leakage by varying α and T_{max} within $\pm\delta_\alpha(E)$ and $\pm\delta_T(E)$, renormalizing the modified profile so that it matches the last layer energy and computing the maximum leakage variation. We find that it varies linearly with $\log_{10} E$ and that the resulting variation of the total reconstructed energy varies linearly with $\log_{10} E$ as $\delta E_{\mathrm{rec}}(E) = 0.025\log_{10}(E/[10\,\mathrm{GeV}])$, which is 5% at 1 TeV. We have checked that saturation does not contribute significantly to this systematic uncertainty, as explained in Appendix A.

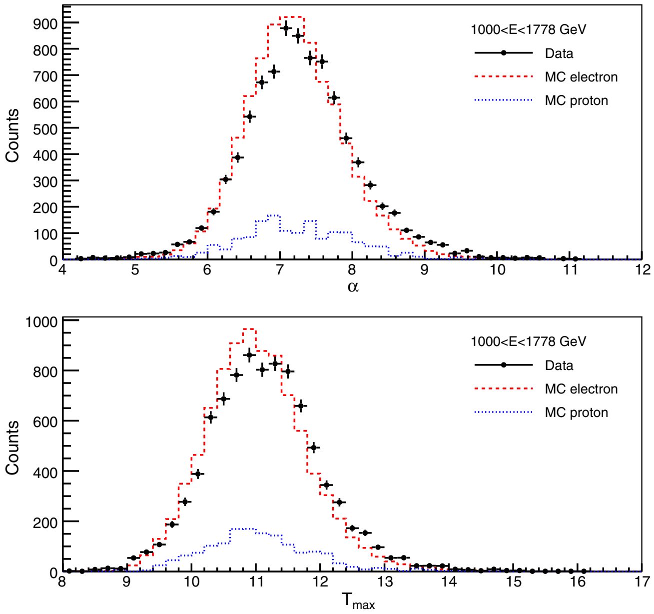

FIG. 11. The shower profile parameters α (top) and T_{max} (bottom) for events between 1 and 1.78 TeV. The contribution from residual background (blue) has been subtracted from the data distributions. The red histograms correspond to the electron simulation.

VI. SYSTEMATIC UNCERTAINTIES

For the HE analysis, we consider four sources of systematic uncertainty. The first three (acceptance, contamination, IVC) relate to the event selection, while the last one is the uncertainty of the energy measurement.

The uncertainty on the acceptance is estimated in each energy bin by measuring the sensitivity of the measured CRE flux to the choice of the cut on P_{CRE} by varying P_{cut} in a range corresponding to a variation in efficiency of ±20% around the nominal efficiency (under the requirement that $P_{\mathrm{cut}} < P_{\mathrm{max}}$). The flux variation, which we attribute to a remaining data/MC disagreement, is found to be less than 2% up to ∼500 GeV, increasing to 6% at 2 TeV.

The number of residual background events is estimated by fitting simulated background templates to the data. In order to take into account the uncertainty of the GEANT4 prediction of the fraction of protons mimicking electromagnetic showers, we assume a 20% uncertainty on the number of background events after the selection cut [30–32]. Due to the small residual background contamination, this uncertainty leads to a change in the number of signal events of less than 2% up to 1 TeV, increasing to 7% at 2 TeV.

For each input variable to the BDT, the IVC corrections are derived from the difference between the peak position of the data and MC distributions. After IVC corrections, there are still some small residual differences. We derive two alternative sets of IVC corrections in which each correction is displaced by plus or minus the maximum of the residual differences at any energy and inclination angle.

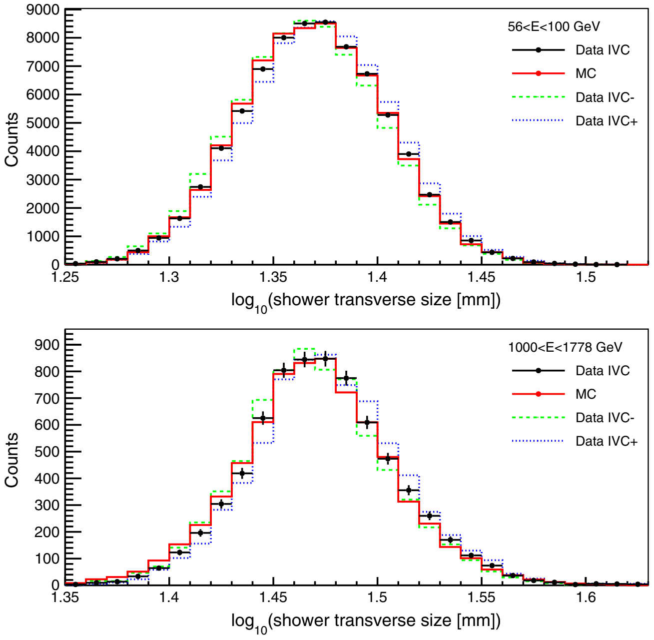

FIG. 12. The logarithm of the shower transverse size after the nominal IVC correction (black) and after moving the correction factors by plus or minus the maximum data/MC residual differences (blue and green) for events between 56 and 100 GeV (top) and between 1 and 1.78 TeV (bottom). The contribution from residual background has been subtracted from the data distributions. The red histograms correspond to the electron simulation.

Figure 12 compares the distributions of the transverse size of the shower obtained with these two sets of corrections to the nominal one and the prediction of the simulation. The variation of the number of signal events compared to the nominal IVC corrections increases from 2% at 42 GeV to 10% at 1 TeV, reaching 14% at 2 TeV.

Regarding the systematic uncertainty on the energy measurement, there are two independent sources of uncertainty as presented in Sec. V. The first one is the systematic uncertainty on the absolute energy scale, which does not depend on energy and is 2%. The second one is the systematic uncertainty on the energy reconstruction and varies linearly with $\log_{10} E$ from 0% at 10 GeV to 5% at 1 TeV.

In order to account for the energy dependent part of the energy measurement systematic uncertainty, we change the energies of all flight-data events according to some conservative scenarios that depend on the spectral hypothesis we test and repeat the whole analysis. Compared to this uncertainty, the constant 2% uncertainty on the absolute energy scale is subdominant and is not considered when fitting the CRE spectrum.

When fitting the CRE spectrum in the HE analysis energy range, we add in quadrature the acceptance uncertainty to the statistical uncertainty and we treat the sum of the contamination and the IVC corrections uncertainties as nuisance parameters, as described in Appendix C. When displaying the spectrum, the statistical and systematic uncertainties (except the one on the energy measurement) are added in quadrature.

For the LE analysis, we consider the acceptance and contamination systematic uncertainties, as well as the changes induced in the spectrum by changing the McIlwain L selection. The sum of these uncertainties is ≤4% and is added in quadrature to the statistical uncertainty.

VII. RESULTS AND DISCUSSION

For both the LE and HE analyses, we fit the CRE count spectrum by forward folding the input flux using the detector response matrix (DRM) in order to take into account the detector energy resolution. The results are shown in Figs. 13 and 15. Tables with fluxes as well as event numbers can be found in Appendix D. The bin-by-bin fluxes are obtained by performing a fit with the DRM in each bin separately with a single power law with a fixed 3.1 spectral index. We note that the LE and HE spectra match very well over the overlapping range $42 < E < 70$ GeV.

The dashed lines illustrate the systematic uncertainty on the energy reconstruction and correspond to the central values of the LAT flux for two scenarios in which the energy is changed by a factor that varies linearly in $\log_{10} E$ between 0% at 10 GeV and ±5% at 1 TeV. We emphasize that these lines do not take into account the statistical uncertainty nor the systematic uncertainties unrelated to the energy measurement.

We also derive the HE spectrum using the subclass of events with a path length in the CAL greater than 12 X_0 introduced in Sec. V. This spectrum is systematically lower

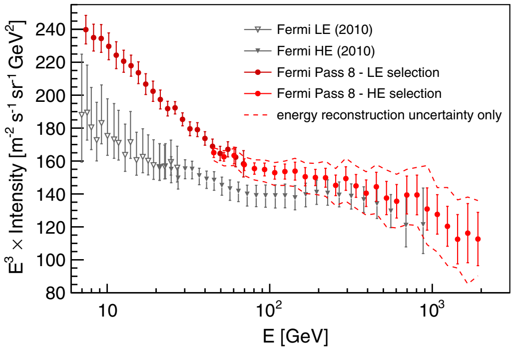

FIG. 13. CRE spectrum between 7 GeV and 2 TeV measured by the LAT and the previous LAT measurement [16]. All error bars represent the quadratic sum of statistical and systematic uncertainties (except the one on the energy measurement). The LAT flux is multiplied by the cube of the representative energy in each bin, computed following Eq. (6) of [33] with an E^{-3} spectrum. The area between the dashed lines corresponds to the uncertainty band due to the LAT energy reconstruction uncertainty only. The 2% systematic uncertainty on the energy scale is not indicated.

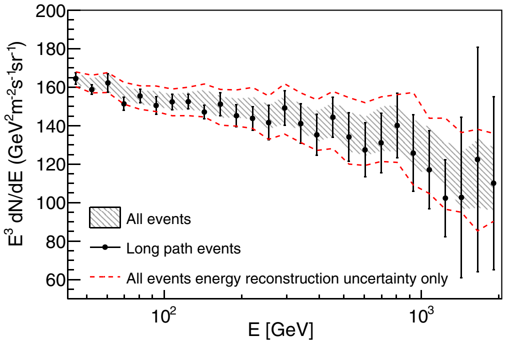

FIG. 14. CRE spectrum between 42 GeV and 2 TeV measured with all events (grey band) and with long-path events (black points). In both cases, the statistical and systematic uncertainties (except for the energy measurement) are added in quadrature. The area between the dashed lines corresponds to the uncertainty band due to the LAT energy reconstruction uncertainty only of the all-event selection.

than but compatible with the all-events spectrum, as can be seen in Fig. 14. Although the energy resolution for the long-path selection is much better, the systematic uncertainties (except the one on the energy measurement) are similar to the ones of the all-events spectrum up to 200 GeV and larger above. Regarding the systematic uncertainty on the energy measurement, the long-path selection spectrum is halfway between the nominal spectrum and the spectrum corresponding to an energy correction of -5% at 1 TeV. It is compatible with the systematic uncertainty on the energy measurement of the long-path selection which is 2.5% at 1 TeV. We conclude that the long-path selection does not allow a more precise measurement of the CRE spectrum but it tends to favor a scenario in which the energy correction is negative rather than positive.

Below 100 GeV, the new LAT measurement differs from the previous one by 10%–30%, as can be seen in Fig. 13. A large part of this difference below 30 GeV is due to the lack of correction in the previous analysis for the loss of CREs above the geomagnetic energy cutoff. After applying this correction, the remaining difference is 10–15% and is due to imperfections in the simulation that was used in the previous analysis (remnants of electronic signals from out-of-time particles were not simulated [34]).

The CRE spectrum between 7 and 42 GeV is well fitted by a power law with a spectral index 3.21 ± 0.02. The low χ^2 (2.25 for 15 degrees of freedom) means that the systematic uncertainties are too large to detect the deviation from a power law due to the magnetic field of the heliosphere. This is strengthened by the fact that fitting between 15 and 42 GeV changes the spectral index by only 0.005. We therefore do not take into account the heliospheric effects in the following fits.

As can be seen in Fig. 15, when not taking into account the uncertainty on the energy reconstruction, the LAT CRE spectrum is above the AMS-02 one for energies larger than ~70 GeV and suggests the presence of a break in the spectrum. Fitting the spectrum between 7 GeV and 2 TeV with a single power law yields $\chi^2 = 64.6$ for 36 degrees of freedom, corresponding to a probability of 2.4×10^{-3}. As expected, a broken power-law fit yields a much lower $\chi^2 = 19.2$ for 34 degrees of freedom. The break energy is 53 ± 8 GeV and the spectral indices below and above the break are 3.21 ± 0.02 and 3.07 ± 0.02, respectively.

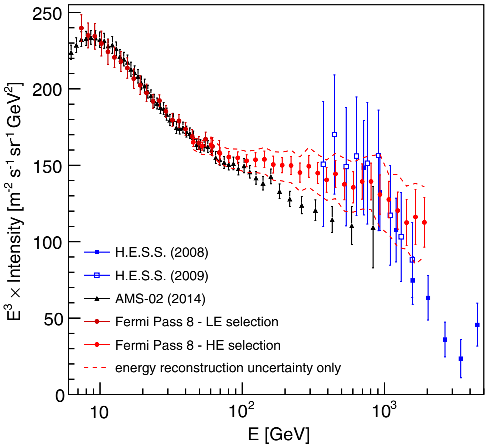

FIG. 15. CRE spectrum between 7 GeV and 2 TeV measured by the LAT along with other recent measurements by AMS-02 [15] and H.E.S.S. [17,18]. All error bars represent the quadratic sum of statistical and systematic uncertainties (except the one on the energy measurement). The LAT flux is multiplied by the cube of the representative energy in each bin, computed following Eq. (6) of [33] with an E^{-3} spectrum. The area between the dashed lines corresponds to the uncertainty band due to the LAT energy measurement uncertainty only. The 2% systematic uncertainty on the energy scale is not indicated.

In order to estimate the influence of the energy measurement systematic uncertainty on the detection of a break, we consider the event-energy rescaling scenario that would be responsible for such a break, among the scenarios allowed by the systematic uncertainty on the energy reconstruction. In this scenario, the energy is unchanged up to 50 GeV and then decreases linearly with $\log_{10} E$ to -5% at 1 TeV. The single power-law fit then yields a $\chi^2 = 49.9$ for 36 degrees of freedom, corresponding to a 6% probability.

This relatively low probability suggests that the broken power-law hypothesis would be preferred. The broken power-law fit, performed with the same scenario, yields indeed a lower $\chi^2 = 28.9$ for 34 degrees of freedom, a break energy of 47 ± 6 GeV and spectral indices below and above the break of 3.21 ± 0.02 and 3.11 ± 0.02, respectively. The χ^2 difference is 21 for two less degrees of freedom. The broken power-law hypothesis is thus preferred at the 4σ level. We note that in all the fits, some of the systematic uncertainties are treated using the nuisance parameter approach. Therefore the χ^2 and corresponding probabilities depend slightly on the number of nuisance parameters but the level of significance of the break does not change.

AMS-02 estimated the lower limit above which the flux is described by a single power law and found 30.2 GeV [15], reporting a spectral index above this energy of $3.170 \pm 0.008(\mathrm{stat}+\mathrm{syst}) \pm 0.008(\text{energy measurement})$. Performing a single power-law fit of the LAT spectrum above the same energy with the energy modification scenario introduced above, we find a spectral index of 3.125 ± 0.020, with a χ^2 of 28.9 for 22 degrees of freedom, corresponding to a 14% probability. Comparing this result to the lower AMS-02 value allowed by the systematic uncertainty on the energy scale, we find that the difference between the Fermi and AMS-02 spectral indices above 30.2 GeV is 0.037 ± 0.022. The difference is at the level of 1.7σ. This could indicate that systematic uncertainties on the energy measurement in one or both of the results are slightly larger than estimated.

At higher energies, H.E.S.S. reported in [17] that, leaving its energy scale factor free, the H.E.S.S. data above 600 GeV combined with earlier data were well reproduced by an exponentially cutoff power law with an index of 3.05 ± 0.02 and a cutoff at 2.1 ± 0.3 TeV. The LAT CRE spectrum above 50 GeV, as indicated by the previous broken power-law fits, is compatible with a single power law with a spectral index of $3.07 \pm 0.02(\mathrm{stat}+\mathrm{syst})$ $\pm 0.04(\text{energy measurement})$. Fitting the count spectrum above 50 GeV with an exponentially cutoff power law $E^{-\gamma}e^{-E/E_c}$ does not yield statistically significant evidence for a cutoff (a χ^2 difference of 1 for 1 less degree of freedom) and we exclude $E_c < 2.1$ TeV at 95% CL. Assuming a scenario in which the energy is changed by 0% at 50 GeV to −5% at 1 TeV, we exclude $E_c < 1.8$ TeV at 95% CL.

Regarding the agreement between the H.E.S.S. and LAT spectra, we note that, as can be seen in Fig. 15, the energy measurement scenario corresponding to the lower dashed line yields a LAT CRE spectrum that connects to H.E.S.S. data around 1 TeV. With this scenario, the LAT spectral index is ~3.11, relatively steeper than 3.05, as reported by H.E.S.S. As a result, a LAT and H.E.S.S. combined fit would lead to a cutoff larger than ~2.1 TeV, well above the LAT lower limit of 1.8 TeV.

The precision of the LAT measurement is limited primarily by the energy dependent systematic uncertainty on the energy measurement, due to the low containment of CRE induced showers in the LAT calorimeter that worsens with energy. A possible way to mitigate this issue would be to use CRE events with an incidence angle greater than 60 degrees. The showers of these events are much more contained in the LAT instrument and the systematic uncertainty on the energy reconstruction would thus be reduced. Unfortunately, the drawback of this approach is that the track information of such events is scarce or inaccurate, which strongly hampers background rejection. We have started to investigate this approach but assessing the improvement that it can lead to is beyond the scope of this paper.

If this approach proves to be successful, its results, along with updated measurements of AMS-02 and H.E.S.S. and the first results of DAMPE [35] and CALET [36], would certainly help in detecting and characterizing precisely the features of the CRE spectrum between 10 GeV and several TeVs.

ACKNOWLEDGMENTS

The *Fermi*-LAT Collaboration acknowledges support for LAT development, operation and data analysis from NASA and DOE (United States), CEA/Irfu and IN2P3/CNRS (France), ASI and INFN (Italy), MEXT, KEK, and JAXA (Japan), and the K. A. Wallenberg Foundation, the Swedish Research Council and the National Space Board (Sweden). Science analysis support in the operations phase from INAF (Italy) and CNES (France) is also gratefully acknowledged. We would like to thank the INFN GRID Data Centers of Pisa, Trieste and CNAF-Bologna, the DOE SLAC National Accelerator Laboratory Computing Division, and the CNRS/IN2P3 Computing Center (CC-IN2P3—Lyon/Villeurbanne) in partnership with CEA/DSM/Irfu for their strong support in performing the massive simulations necessary for this work. W. Mitthumsiri is partially supported by the Thailand Research Fund (Grants No. TRG5880173 and No. RTA5980003).

APPENDIX A: ENERGY RECONSTRUCTION

The LAT energy reconstruction above ~5 GeV is performed by fitting the shower profile, using the eight CAL layer energies. We use the following representation of the longitudinal shower profile [37],

$$\frac{dE(t)}{dt} = E \times \mathcal{P}(\alpha,\beta,t) = E \times \frac{(\beta t)^{\alpha-1}\beta e^{-\beta t}}{\Gamma(\alpha)}, \qquad \text{(A1)}$$

where t is the longitudinal shower depth in units of radiation length, α the shape parameter, and β the scaling parameter. The profile shape $\mathcal{P}$ is such that $\int \mathcal{P}(\alpha,\beta,t)dt = 1$ and its maximum for given values of α and β is reached at $T_{\max} = (\alpha-1)/\beta$. The profile fit has three parameters (the energy and two shape parameters) and 5 degrees of freedom.

We use a model of the longitudinal profile (mean and standard deviation of the shape parameters) and a model of the average radial profile of electromagnetic showers in CsI. Both models describe the variation of the longitudinal and radial profiles with energy and were derived using dedicated GEANT4 simulations from 1 GeV to 3 TeV.

The profile fit fully takes into account the geometry of the LAT calorimeter (especially the gaps between modules) in order to predict the energy deposited in the layers and crystals for any given shower profile. The energy deposition prediction is performed on an event-by-event basis, by going forward along the event axis (measured with the tracker) in steps of 1.85 mm ($0.1X_0$). At each step, we compute the fraction of energy deposited in each crystal, taking into account the shower longitudinal and radial profiles and the calorimeter geometry.

The fraction of energy deposited in the crystals as a function of distance along the event axis is translated into a fraction of deposited energy as a function of radiation length, which is used in the profile fit to compute the layer energies that are compared to the measured ones. It is to be noted that the longitudinal profile is free to fluctuate in the fit according to the model of the longitudinal profile derived with GEANT4. This is done by adding to the χ^2 a gaussian prior for each of the shape parameters, with mean and standard deviation as given by the model of the longitudinal profile. More information can be found in [38].

Pass 8 introduces several improvements to the energy reconstruction:

(i) the upper end of the energy range over which the shower longitudinal and radial models have been computed has been increased from 150 GeV to 3 TeV;

(ii) the widening of the radial profile in the gaps between modules has been modeled;

(iii) in the Pass 6/7 version of the profile fit, layers with at least one saturated crystal were discarded. In Pass 8, only the saturated crystals are discarded: for each layer, the energy that is considered in the fit is the sum of the energy of the nonsaturated crystals.

The last point must be taken into account when estimating the systematic uncertainty on the energy reconstruction presented in Sec. V. The energy deposited in the saturated crystals is missed and this additional leakage amounts on average to 10% at 1 TeV, increasing to 25% at 2 TeV. Saturation occurs for crystals in the core of the shower. Therefore, the predicted energy for the layers with saturated crystals depends on the radial profile model that we use.

In order to quantify the dependence of the energy reconstrution on the radial profile model, we scale it by ±20%. As expected, scaling the radial profile changes the χ^2 of the fit but we find that this variation occurs only above ~800 GeV, that is to say when crystal saturation is important. Below ~800 GeV, the χ^2 is unchanged. The comparison of the $\log_{10}\chi^2$ between data and MC shows that the data/MC difference increases linearly with $\log_{10} E$, from 0 at 10 GeV to 0.13 at 1 TeV, without any sharp variation around 800 GeV. Quantitatively, the variation of this data/MC difference between 800 GeV and 1 TeV is less than 0.05, which would correspond to a 5% scaling of the radial profile. We therefore conclude that the radial profile model we use is correct within 5%. When scaling the radial profile within 5%, we find that the reconstructed energy variation is smaller than $0.1\delta E_{\rm rec}(E)$ and conclude that saturation does not significantly contribute to the systematic uncertainty on the energy reconstruction.

APPENDIX B: MEASUREMENT OF THE ABSOLUTE ENERGY SCALE AT ~10 GeV

The geomagnetic cutoff in the CRE spectrum provides a spectral feature that allows an absolute calibration of the LAT energy scale. A previous measurement of the geomagnetic cutoff was used to calibrate the LAT energy scale based on one year of LAT data [29]. We performed the same analysis, using almost seven years of Pass 8 data, in six McIlwain L intervals. We used the LE CRE estimator with a cut ensuring a constant 2% residual background contamination. The $P_{\rm CRE}$ cut efficiency for electrons is ~30% below 5 GeV, rising to 90% at 10 GeV. In order to check the sensitivity of the measurements to the selection, we also used a selection ensuring a constant 5% residual background contamination, which corresponds to an efficiency of 70% below 5 GeV, rising to 95% at 10 GeV.

After background subtraction, we are left with primary and secondary electrons. In order to measure the fraction of secondaries, we fit the CRE azimuthal distribution with the sum of two templates: for primary CREs, we use the one predicted by the tracer and, for secondary electrons, we use the one observed in data well below the rigidity cutoff (when the primary fraction is lower than 0.5%). Figure 16

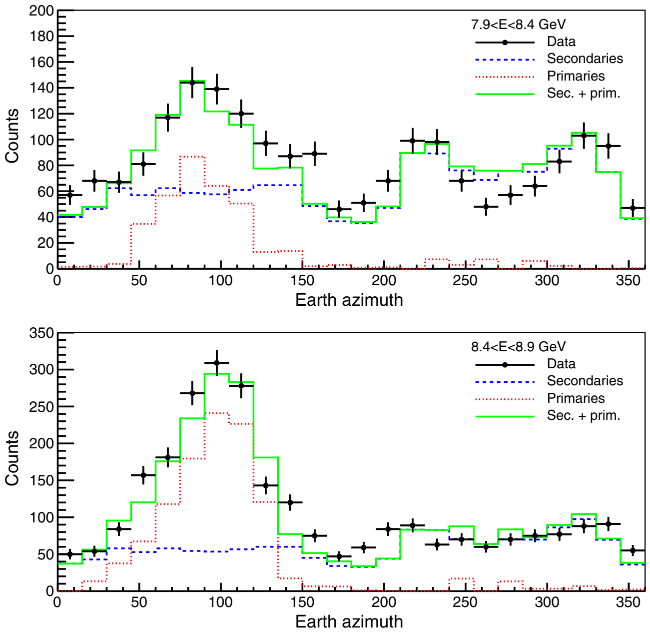

FIG. 16. Examples of the template fit of the azimuthal distribution for McIlwain L in [1.0, 1.1]: events between 7.9 and 8.4 GeV (top) and between 8.4 and 8.9 GeV (bottom). The black, red, blue and green histograms correspond to data, the secondary template, the primary template, and the sum of the secondary and primary templates. North and East correspond to 0 and 90°, respectively.

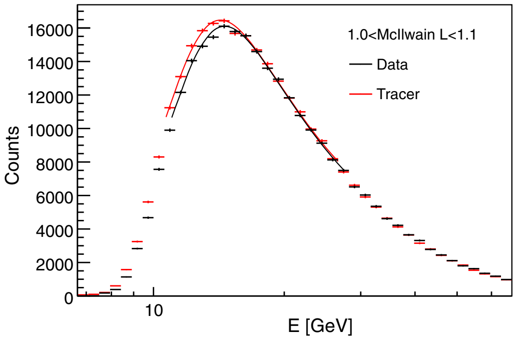

FIG. 17. Measured count spectrum (black) of primary CREs after removal of secondary electrons for the McIlwain L interval [1.0, 1.1], and the count spectrum predicted by the tracer. The latter is normalized so that its integral above 20 GeV is the same as in the data.

shows two examples of such fits for McIlwain L in [1.0, 1.1]. They correspond to two adjacent energy bins below the geomagnetic cutoff, in which the primary fraction increases from 20% to 45%.

For each McIlwain L interval, we fit for the contribution of secondaries as a function of energy and subtract it to obtain the count spectrum of primary CRE. We fit the count spectrum with $E^{-\gamma_p}/(1+(E/E_c)^{-\alpha})$, where E_c is the cutoff and γ_p is the spectral index above E_c. We modify the tracer input spectrum according to solar modulation, using the force field approximation with a solar modulation parameter ϕ set to an average value for the 2008–2015 period of 500 MV. Figure 17 shows the result of the fit for the McIlwain L interval [1.0, 1.1]. We then compare the values of E_c obtained in the data and predicted by the tracer to check the LAT absolute energy scale.

The $E_c^{\mathrm{data}}/E_c^{\mathrm{tracer}}$ ratios in the six McIlwain L intervals are in agreement, as shown in Fig. 18, and the average ratio is 1.033 ± 0.004. We varied the parameters of the analysis (event selection, energy interval used to derive the template of secondaries and spectral index of the tracer spectrum) and found that the average ratio did not vary by more than 0.3%. Using the IGRF 1995 model changed the result by less than 0.1%. We performed this analysis in various time periods and the ratio was constant within less than 1%. We also changed the solar modulation parameter ϕ to 0 and 1000 MV and the ratio changed by 0.5%. We thus estimate the systematic uncertainty of the ratio measurement to be 2%. The previous LAT measurement of the absolute energy scale found an average ratio of $1.025 \pm 0.005(\mathrm{stat}) \pm 0.025(\mathrm{syst})$, which is compatible with the new result.

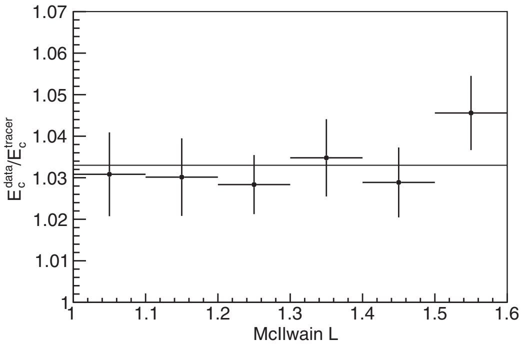

FIG. 18. The $E_c^{\mathrm{data}}/E_c^{\mathrm{tracer}}$ ratio as a function of McIlwain L. The horizontal line corresponds to the average ratio.

APPENDIX C: SYSTEMATIC UNCERTAINTIES AS NUISANCE PARAMETERS

The potential systematic bias in the CRE flux measurement induced by the systematic uncertainties on background subtraction and the IVC corrections can be modeled as a sequence of unknown correction factors. They correspond to nuisance parameters that are derived in the fit of the CRE spectrum when we test different parameterizations for the CRE spectrum.

We define $\mathcal{S}(E)$ as the quadratic sum of the contamination and IVC corrections systematic uncertainties (discussed in Sec. VI) as a function of energy. We choose $\mathcal{N}$ reference energies $\mathcal{E}_j$, logarithmically spaced between 42 GeV and 2 TeV, in order to define $s(E;\mathbf{w})$, a piecewise function, linear in $\log_{10} E$, defined by its values w_j at $\mathcal{E}_j$. The set of w_j are the nuisance parameters. The correction factor for the predicted number of counts in the analysis energy bin i is $1 + s(E_i;\mathbf{w})\mathcal{S}(E_i)$ and the χ^2 function for the spectral fit is given by

$$\chi^2 = \sum_{i=1}^{n}\left(\frac{N_i - [1 + s(E_i;\mathbf{w})\mathcal{S}(E_i)]\mu_i(\boldsymbol{\theta})}{\delta N_i}\right)^2 + \sum_{j=1}^{\mathcal{N}} w_j^2, \tag{C1}$$

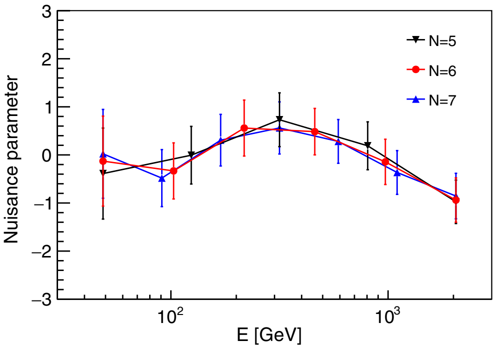

FIG. 19. Nuisance parameters found by the fit of the CRE spectrum between 50 GeV and 2 TeV for various numbers of reference energies: $\mathcal{N} = 5$ (black), 6 (red), and 7 (blue).

where $\boldsymbol{\theta}$ are the free parameters of the CRE spectral model, n is the number of energy bins of the analysis, N_i is the number of counts measured in bin i, μ_i is the predicted number of counts after convolution with the DRM and δN_i is the quadratic sum of the statistical and acceptance uncertainties. The second term of the χ^2 function corresponds to a Gaussian prior on the amplitude of the nuisance parameters.

The choice of the number of nuisance parameters $\mathcal{N}$ cannot be inferred from first principles. Between the contamination and the IVC corrections systematic uncertainties, the latter dominates. Because we build eight BDTs, the importance of the BDT input variables can change from bin to bin. As a consequence, a change of the IVC correction for one observable can have a significantly different impact even on two adjacent BDT energy bins.

Ignoring any correlation between BDT energy bins would lead to the choice $\mathcal{N} = 8$. But the importance of the input variables depends on the variation of the event topology with energy, which is not expected to change abruptly at the BDT energy boundaries. And this argument also applies for the contamination uncertainty. In order to take into account the BDT bin-to-bin correlation, we chose $\mathcal{N} = 6$. We checked that the fit results do not change significantly with $\mathcal{N} = 5$ or 7.

When fitting the CRE spectrum between 50 GeV and 2 TeV with a single power law and $\mathcal{N} = 6$, we find $\chi^2 = 15.5$ for 18 degrees of freedom. The nuisance parameters values found by the fitting procedure are shown in Fig. 19, as well as those found with $\mathcal{N} = 5$ and 7. In all three cases, the nuisance parameters are within ± 1 and the spectral index is 3.07 ± 0.02.

When fitting with an exponentially cutoff power law $E^{-\gamma} e^{-E/E_c}$, the 95% CL lower limit on the energy cutoff for $\mathcal{N} = 5$, 6 and 7 is 2.18, 2.13, and 2.19, respectively.

APPENDIX D: TABLES

Tables I and II give the number of events, the residual background contamination, and the CRE flux in each energy bin for the LE and HE analyses, respectively. These tables are available in machine-readable format at https://www-glast.stanford.edu/pub_data/1144.

TABLE I. Number of events after background subtraction (without correction for the loss of CREs above the geomagnetic energy cutoff), residual background contamination and flux J_E, with its statistical and systematic errors, for the LE selection.

Energy (GeV)	Counts	Contamination	J_E (GeV^{-1} s^{-1} m^{-2} sr^{-1})
7.0–7.8	8231	0.02	$5.93\times\,(1 \pm 0.016 \pm 0.032)\,\times 10^{-01}$
7.8–8.7	35912	0.02	$4.18\times\,(1 \pm 0.008 \pm 0.034)\,\times 10^{-01}$
8.7–9.7	51417	0.02	$3.02\times\,(1 \pm 0.007 \pm 0.035)\,\times 10^{-01}$
9.7–10.8	60019	0.03	$2.15\times\,(1 \pm 0.007 \pm 0.035)\,\times 10^{-01}$
10.8–12.0	66545	0.03	$1.53\times\,(1 \pm 0.007 \pm 0.036)\,\times 10^{-01}$
12.0–13.3	74725	0.02	$1.09\times\,(1 \pm 0.007 \pm 0.030)\,\times 10^{-01}$
13.3–14.8	84090	0.03	$7.90\times\,(1 \pm 0.007 \pm 0.029)\,\times 10^{-02}$
14.8–16.4	89109	0.03	$5.67\times\,(1 \pm 0.007 \pm 0.030)\,\times 10^{-02}$
16.4–18.2	81203	0.03	$4.02\times\,(1 \pm 0.007 \pm 0.030)\,\times 10^{-02}$
18.2–20.2	68111	0.03	$2.88\times\,(1 \pm 0.008 \pm 0.029)\,\times 10^{-02}$
20.2–22.4	56832	0.03	$2.06\times\,(1 \pm 0.008 \pm 0.028)\,\times 10^{-02}$
22.4–24.8	46535	0.03	$1.47\times\,(1 \pm 0.009 \pm 0.022)\,\times 10^{-02}$
24.8–27.6	38267	0.03	$1.07\times\,(1 \pm 0.010 \pm 0.017)\,\times 10^{-02}$
27.6–30.7	30449	0.03	$7.54\times\,(1 \pm 0.011 \pm 0.018)\,\times 10^{-03}$
30.7–34.1	23408	0.04	$5.33\times\,(1 \pm 0.013 \pm 0.020)\,\times 10^{-03}$
34.1–37.9	18867	0.04	$3.87\times\,(1 \pm 0.014 \pm 0.019)\,\times 10^{-03}$
37.9–42.2	14718	0.05	$2.72\times\,(1 \pm 0.016 \pm 0.017)\,\times 10^{-03}$
42.2–47.0	11186	0.05	$1.92\times\,(1 \pm 0.019 \pm 0.018)\,\times 10^{-03}$
47.0–52.3	8618	0.06	$1.35\times\,(1 \pm 0.021 \pm 0.015)\,\times 10^{-03}$
52.3–58.5	6942	0.05	$9.89\times\,(1 \pm 0.023 \pm 0.015)\,\times 10^{-04}$
58.5–65.3	5165	0.05	$6.89\times\,(1 \pm 0.027 \pm 0.024)\,\times 10^{-04}$
65.3–73.0	3891	0.08	$4.82\times\,(1 \pm 0.034 \pm 0.038)\,\times 10^{-04}$

TABLE II. Number of events after background subtraction, residual background contamination and flux J_E, with its statistical and systematic errors (the acceptance uncertainty and the sum of the contamination and IVC correction uncertainties are shown separately), for the HE selection.

Energy (GeV)	Counts	Contamination	J_E (GeV^{-1} s^{-1} m^{-2} sr^{-1})
42.2–48.7	3948132	0.02	$1.78\times\ (1 \pm 0.001 \pm 0.012 \pm 0.013)\ \times 10^{-03}$
48.7–56.2	2945632	0.02	$1.14\times\ (1 \pm 0.001 \pm 0.008 \pm 0.014)\ \times 10^{-03}$
56.2–64.9	2189648	0.02	$7.42\times\ (1 \pm 0.002 \pm 0.027 \pm 0.016)\ \times 10^{-04}$
64.9–75.0	1609640	0.02	$4.66\times\ (1 \pm 0.001 \pm 0.016 \pm 0.017)\ \times 10^{-04}$
75.0–86.6	1161424	0.03	$2.98\times\ (1 \pm 0.002 \pm 0.009 \pm 0.020)\ \times 10^{-04}$
86.6–100.0	865855	0.03	$1.93\times\ (1 \pm 0.002 \pm 0.012 \pm 0.022)\ \times 10^{-04}$
100.0–115.5	629884	0.03	$1.24\times\ (1 \pm 0.002 \pm 0.012 \pm 0.023)\ \times 10^{-04}$
115.5–133.4	466148	0.03	$8.06\times\ (1 \pm 0.002 \pm 0.016 \pm 0.025)\ \times 10^{-05}$
133.4–154.0	343066	0.04	$5.24\times\ (1 \pm 0.002 \pm 0.021 \pm 0.029)\ \times 10^{-05}$
154.0–177.8	253798	0.04	$3.33\times\ (1 \pm 0.003 \pm 0.013 \pm 0.034)\ \times 10^{-05}$
177.8–205.4	187997	0.04	$2.16\times\ (1 \pm 0.003 \pm 0.015 \pm 0.029)\ \times 10^{-05}$
205.4–237.1	138234	0.05	$1.40\times\ (1 \pm 0.003 \pm 0.020 \pm 0.032)\ \times 10^{-05}$
237.1–273.8	101444	0.05	$8.80\times\ (1 \pm 0.004 \pm 0.016 \pm 0.040)\ \times 10^{-06}$
273.8–316.2	75547	0.06	$5.88\times\ (1 \pm 0.005 \pm 0.014 \pm 0.045)\ \times 10^{-06}$
316.2–365.2	54462	0.06	$3.70\times\ (1 \pm 0.005 \pm 0.018 \pm 0.044)\ \times 10^{-06}$
365.2–421.7	37883	0.07	$2.33\times\ (1 \pm 0.006 \pm 0.019 \pm 0.054)\ \times 10^{-06}$
421.7–487.0	28142	0.07	$1.56\times\ (1 \pm 0.007 \pm 0.007 \pm 0.060)\ \times 10^{-06}$
487.0–562.3	19641	0.08	$9.62\times\ (1 \pm 0.008 \pm 0.016 \pm 0.071)\ \times 10^{-07}$
562.3–649.4	14000	0.07	$6.16\times\ (1 \pm 0.009 \pm 0.033 \pm 0.067)\ \times 10^{-07}$
649.4–749.9	10240	0.06	$4.11\times\ (1 \pm 0.010 \pm 0.042 \pm 0.070)\ \times 10^{-07}$
749.9–866.0	7338	0.08	$2.67\times\ (1 \pm 0.012 \pm 0.024 \pm 0.082)\ \times 10^{-07}$
866.0–1000.0	4938	0.10	$1.63\times\ (1 \pm 0.015 \pm 0.024 \pm 0.094)\ \times 10^{-07}$
1000.0–1154.8	3406	0.11	$1.03\times\ (1 \pm 0.018 \pm 0.028 \pm 0.088)\ \times 10^{-07}$
1154.8–1333.5	2249	0.15	$6.31\times\ (1 \pm 0.023 \pm 0.016 \pm 0.097)\ \times 10^{-08}$
1333.5–1539.9	1491	0.13	$3.83\times\ (1 \pm 0.027 \pm 0.075 \pm 0.107)\ \times 10^{-08}$
1539.9–1778.3	1086	0.19	$2.57\times\ (1 \pm 0.036 \pm 0.047 \pm 0.143)\ \times 10^{-08}$
1778.3–2053.5	737	0.22	$1.62\times\ (1 \pm 0.039 \pm 0.077 \pm 0.115)\ \times 10^{-08}$

---

[1] J. Nishimura, M. Fujii, and T. Taira, *International Cosmic Ray Conference* 1, 488 (1979).

[2] O. Adriani *et al.*, Nature (London) **458**, 607 (2009).

[3] M. Ackermann *et al.* (Fermi-LAT Collaboration), Phys. Rev. Lett. **108**, 011103 (2012).

[4] L. Accardo *et al.* (AMS Collaboration), Phys. Rev. Lett. **113**, 121101 (2014).

[5] M. Ackermann *et al.* (Fermi-LAT Collaboration), Phys. Rev. D **82**, 092003 (2010).

[6] C. S. Shen, Astrophys. J. **162**, L181 (1970).

[7] J. Nishimura, M. Fujii, T. Taira, E. Aizu, H. Hiraiwa, T. Kobayashi, K. Niu, I. Ohta, R. L. Golden, and T. A. Koss, Astrophys. J. **238**, 394 (1980).

[8] J. Nishimura, T. Kobayashi, Y. Komori, and K. Yoshida, Adv. Space Res. **19**, 767 (1997).

[9] F. A. Aharonian, A. M. Atoyan, and H. J. Voelk, Astron. Astrophys. **294**, L41 (1995).

[10] T. Kobayashi, Y. Komori, K. Yoshida, and J. Nishimura, Astrophys. J. **601**, 340 (2004).

[11] P. Blasi, Phys. Rev. Lett. **103**, 051104 (2009).

[12] I. Cholis, L. Goodenough, D. Hooper, M. Simet, and N. Weiner, Phys. Rev. D **80**, 123511 (2009).

[13] M. Cirelli, M. Kadastik, M. Raidal, and A. Strumia, Nucl. Phys. **B813**, 1 (2009); **B873**, 530 (2013).

[14] L. Bergstrom, J. Edsjo, and G. Zaharijas, Phys. Rev. Lett. **103**, 031103 (2009).

[15] M. Aguilar *et al.* (AMS Collaboration), Phys. Rev. Lett. **113**, 221102 (2014).

[16] M. Ackermann *et al.* (Fermi-LAT Collaboration), Phys. Rev. D **82**, 092004 (2010).

[17] F. Aharonian *et al.* (H.E.S.S. Collaboration), Phys. Rev. Lett. **101**, 261104 (2008).

[18] F. Aharonian *et al.* (H.E.S.S. Collaboration), Astron. Astrophys. **508**, 561 (2009).

[19] M. Di Mauro, F. Donato, N. Fornengo, R. Lineros, and A. Vittino, J. Cosmol. Astropart. Phys. 04 (2014) 006.

[20] W. B. Atwood *et al.* (Fermi-LAT Collaboration), Astrophys. J. **697**, 1071 (2009).

[21] W. Atwood *et al.* (Fermi-LAT Collaboration), arXiv: 1303.3514.

[22] S. Abdollahi *et al.* (Fermi-LAT Collaboration), Phys. Rev. Lett. **118**, 091103 (2017).

[23] M. Di Mauro *et al.* (Fermi-LAT Collaboration), arXiv: 1703.00460.

[24] A. Hocker *et al.*, *Proc. Sci.*, ACAT2007 (2007) 040 [arXiv: physics/0703039].

[25] S. Agostinelli *et al.* (Geant4 Collaboration), Nucl. Instrum. Methods Phys. Res., Sect. A **506**, 250 (2003).

[26] T. Mizuno, T. Kamae, G. Godfrey, T. Handa, D. J. Thompson, D. Lauben, Y. Fukazawa, and M. Ozaki, Astrophys. J. **614**, 1113 (2004).

[27] D. F. Smart and M. A. Shea, Adv. Space Res. **36**, 2012 (2005).

[28] C. C. Finlay *et al.*, Geophys. J. Int. **183**, 1216 (2010).

[29] M. Ackermann *et al.* (Fermi-LAT Collaboration), Astropart. Phys. **35**, 346 (2012).

[30] J. Yarba, J. Phys. Conf. Ser. **396**, 022060 (2012).

[31] A. Dotti (Geant4 Hadronic Working Group, Electromagnetic Working Group Collaboration), in *Proceedings, International Conference on Calorimetry for the High Energy Frontier (CHEF 2013)* (2013), p. 247.

[32] B. Bilki *et al.* (CALICE Collaboration), J. Instrum. **10**, P04014 (2015).

[33] G. D. Lafferty and T. R. Wyatt, Nucl. Instrum. Methods Phys. Res., Sect. A **355**, 541 (1995).

[34] M. Ackermann *et al.* (Fermi-LAT Collaboration), Astrophys. J. Suppl. Ser. **203**, 4 (2012).

[35] F. Gargano (DAMPE Collaboration), in *25th European Cosmic Ray Symposium (ECRS 2016) Turin, Italy, 2016* (2017) arXiv:1701.05046.

[36] P. S. Marrocchesi (CALET Collaboration), J. Phys. Conf. Ser. **718**, 052023 (2016).

[37] E. Longo and I. Sestili, Nucl. Instrum. Methods **128**, 283 (1975), **135**, 587 (1976).

[38] P. Bruel, J. Phys. Conf. Ser. **404**, 012033 (2012).

Journal of Physics: Conference Series

Search for Galactic dark matter from γ-ray spectral lines with *Fermi*-LAT data

To cite this article: Natthakan Thanapreechanan 2017 *J. Phys.: Conf. Ser.* **901** 012002

Search for Galactic dark matter from γ-ray spectral lines with *Fermi*-LAT data

Natthakan Thanapreechanan

Department of Physics, Mahidol University, Thailand

E-mail: `natthakan.thn@student.mahidol.ac.th`

Abstract. Most of the matter in the universe is invisible and is known as dark matter (DM). Weakly Interacting Massive Particles (WIMPs) are possible theoretical candidates for DM. Hypothetically, WIMPs can be detected indirectly by their annihilation or decay products. A possible product is a γ ray. Many DM profile models predict a higher density of WIMPs near the Galactic center. Here we search for monochromatic γ-ray emission from the Galactic center region in data from the Large Area Telescope (LAT), the main instrument onboard the *Fermi* Gamma-ray Space Telescope. We present the preliminary results of the analysis of γ-ray spectral lines to search for DM annihilation and decay signals using the latest version of the LAT data.

1. Introduction

Many studies in cosmology and astrophysics provide evidence of the existence of dark matter (DM) (see, e.g., [1, 2]). Observations of the dynamics of galaxies in a cluster and the rotational velocities of a galaxy imply that there is more mass in the cluster or the galaxy than what can be detected electromagnetically [3–5]. Observation of the Bullet Cluster by weak lensing indicates that DM can be described as particles with low interaction cross section with ordinary matter [6, 7]. Moreover, the cosmic microwave background measurement constrains the DM density in the Universe [8]. Many possible hypothetical candidates for DM exist, including Weakly Interacting Massive Particles (WIMPs) thermally produced in the early universe [1, 2, 9]. Theoretically WIMPs could be observed via WIMP-nucleon scattering in underground experiments, could be produced by a collision of particles in the collider, or could also contribute to cosmic ray (CR) fluxes by their annihilation or decay [10]. Among various candidate particles produced by WIMP annihilation or decay, γ rays are interesting because their propagation is unperturbed by the interstellar magnetic field and preserves spatial information about their sources.

Typical astrophysical sources emit a broad spectral shape in $\sim$GeV range γ rays, which can usually be well approximated as a power law with a high-energy cutoff. Sharp spectral features in this energy range are not expected from any known sources, but could originate from the annihilation or decay of nonrelativistic particles in the $\sim$GeV–TeV mass range. Therefore, the search for γ-ray spectral lines has been employed as one possible tool for DM detection [11, 12].

Since June 2008, the *Fermi* Large Area Telescope (LAT), which is the main instrument on the *Fermi* Gamma Ray Space Telescope (*Fermi*), has been continuously observing the γ-ray sky in the energy range from about 20 MeV to more than 300 GeV. The LAT may be sensitive to γ rays produced from WIMP annihilation or decay. We use 8 years of public data with the most recent event selection version of the LAT data (Pass 8 Clean) to search for spectral lines between 50–290 GeV in many regions of interest.

2. Method

2.1. Regions of interest

The regions of interest (ROIs) are defined as circular regions of the sky with different angular radii centered at the Galactic center (GC). Each region is optimized for different profiles of the DM distribution in the Galaxy (i.e., Navarro-Frenk-White profile (NFW), contracted NFW profile (NFWc), Einasto profile, and the core isothermal profile). The details of the optimization procedure are described in [14] in appendix B. The names of five ROIs used in this analysis come from the values of the radius that they subtend, e.g., R3 for $r = 3^\circ$. R3 (optimized for NFWc), R16 (optimized for Einasto), R41 (optimized for NFW), and R90 (optimized for core isothermal) are more sensitive to WIMP annihilation, while R180 is more sensitive to the WIMP decay [15]. In addition, we mask out the Galactic plane (GP) ($| b | < 5^\circ$ and $| l | > 6^\circ$) where γ-ray emission from astrophysical sources is very bright and can obscure the faint DM signals. Although both R3 and R16 also contain high-concentration of astrophysical sources similar to the GP, DM particles which only interact gravitationally are predicted to clump together more densely near the GC. Therefore, the fraction of DM signals to the astrophysical background in R3 and R16 may be higher in than that in the GP.

We use the Earth limb (EL) and the GP (excluding the GC), which we call the inverse ROI, as control regions. The γ-ray emission from the EL is produced by CRs interacting with the Earth's upper atmosphere, resulting in an extremely bright γ-ray ring as viewed by *Fermi* due to its proximity [16]. The inverse ROI contains various types of γ-ray sources, so it provides good statistics of the astrophysical background. The γ-ray emission in the inverse ROI is also dominated by astrophysical sources and the diffuse emission due to CRs interacting with interstellar medium. Thus, we do not expect to detect any DM signals in these control regions.

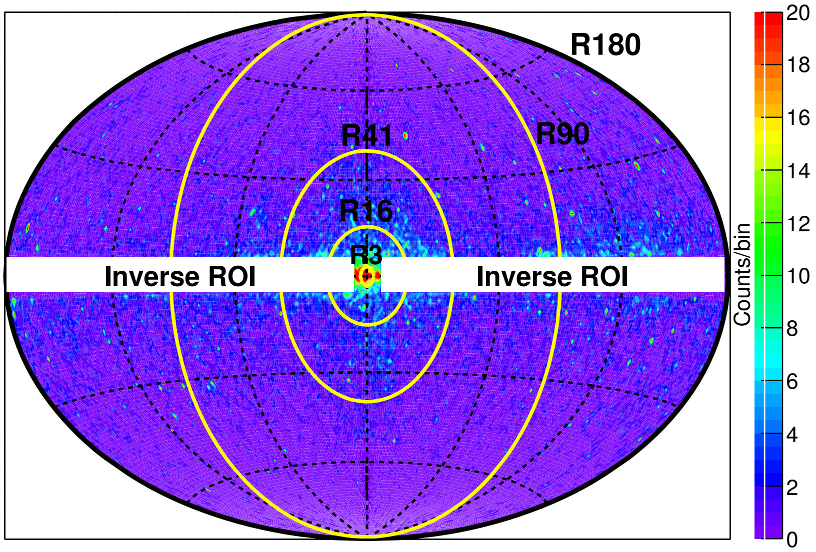

Figure 1: Counts map of 40–300 GeV photons in the Galactic coordinates plotted in the Aitoff projection. The ROIs (R3, R16, R41, R90, and R180) are shown. The inverse ROI (white area) has been masked out here.

2.2. Data selection

We use the latest version of data (Pass 8) [13] developed by the LAT Collaboration. We use 8 years *Fermi*-LAT data (August 2008 – August 2016) with the “Clean” event selection between 40–300 GeV to search for spectral lines between 50 and 290 GeV. In addition, In addition, we avoid contaminations from the bright EL emission by selecting photons with zenith angle smaller than 100°, where the zenith angle is the angle between the originated location of a photon and the zenith direction from the LAT's point of view. It is important to note that the LAT energy resolution between 40–300 GeV is about 5–8%.

2.3. Fitting procedure

To search for γ-ray lines, we perform a maximum likelihood fit in the selected energy range for each of the 5 ROIs. We use 130 energy bins with equal width across the fit energy range, so the bin width is comparable to or smaller than the LAT energy resolution. We define the functional form for the background photon count spectrum as

$$F_{\mathrm{Bg}}(E) = N_{\mathrm{Bg}} E^{-\Gamma_{\mathrm{Bg}}}$$

We define the functional form for the DM signal as a narrow Gaussian shape:

$$F_{\mathrm{DM}}(E) = N_{\mathrm{DM}} \exp\left(- \frac{(E - E_\gamma)^2}{2w^2} \right)$$

where E_γ is the line energy which is varied between 50–290 GeV, and N_{DM} and w are free model parameters. From the instrument's energy resolution, w is constrained to be between 5–8% of E_γ. The best-fit parameters are obtained by performing a maximum likelihood analysis of the measurement data and the $F_{\mathrm{Bg}} + F_{\mathrm{DM}}$ model. The likelihood function is $\mathcal{L} \equiv \prod_{\mathrm{i}}^{\mathrm{N}} P(o_{\mathrm{i}} \mid m_{\mathrm{i}})$, where $P(o_{\mathrm{i}} \mid m_{\mathrm{i}})$ is the Poisson probability of observing o_{i} counts given that the model predicts m_{i} counts in each energy bin i. We vary the fitting parameters of the power law (background) and the Gaussian (DM signal) to determine the maximum likelihood. The significance (s) of the line signal at E_γ is derived from the square-root of the test statistic (TS) : $s = \sqrt{TS} = (2 \ln \frac{\mathcal{L}^{\mathrm{Bg+DM}}}{\mathcal{L}^{\mathrm{Bg}}})^{\frac{1}{2}}$ where $\mathcal{L}^{\mathrm{Bg+DM}}$ is the maximum likelihood from the background+DM signal hypothesis, and $\mathcal{L}^{\mathrm{Bg}}$ is that for only the background hypothesis (without DM signal).

3. Results & Discussion

We perform a search for γ-ray lines in the energy range 50–290 GeV in the five ROIs and two control regions. The signal significance values from fitting spectral lines at various energies in all regions are shown in Figure 2. The calculated statistical significances for all the ROIs and the line energies are below 3.0σ. In high-energy particle physics, a statistical significance less than 3.0σ is considered consistent with background fluctuation. Thus, we find no evidence of significant lines between 50–290 GeV. Figure 2 shows the count spectrum and fit results for R180 with the line energy at 90 GeV, where we observe the largest significance ($s = 1.8\sigma$). We check the influence of the arbitrarily chosen energy bin width of 2.0 GeV used in our analysis by varying the energy bin width among these values: 0.5, 1.0, 1.5, 2.0, 4.0, and 8.0 GeV. All fit results give significances less than 2.0σ.

We examine two control regions which are expected to contain no DM signal and find no lines with $s > 3.0\sigma$ in this energy range. Figure 2 shows the count spectrum fit at 90 GeV using EL and the inverse ROI data, which indicate 0.0σ and 0.0σ. The γ-ray spectra from the control regions can therefore be concluded as featureless. This excludes the possibility that the instrumental effect is responsible for any spectral line in the ROIs.

We have performed a search for γ-ray lines from 50–290 GeV in the five ROIs which are optimized for various DM density profiles, using 8 years of *Fermi*-LAT Pass 8 data. We find no

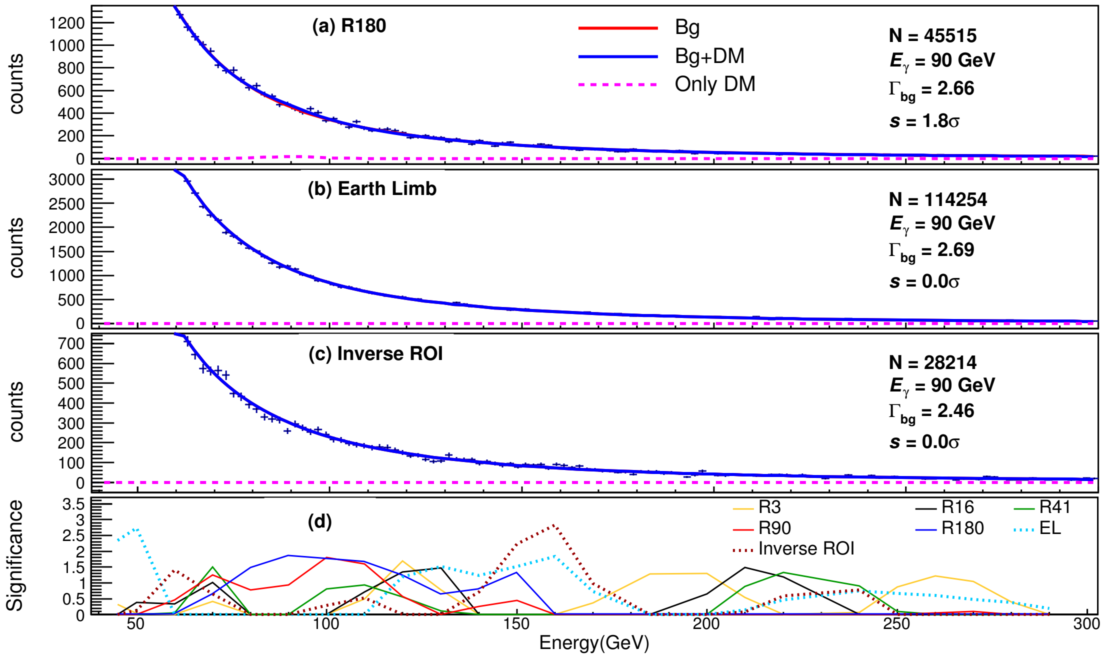

Figure 2: Fit results at 90 GeV line energy in R180 (a), the Earth limb (b), and the inverse ROI (c) are shown. The significance value as a function of line energy from the analyses of count spectra from five ROIs and two control regions are summarized in (d).

significant spectral lines in all ROIs. Our analyses in the control regions, the EL and the inverse ROI, show no significant sharp spectral feature. We will expand the search to a wider energy range in the future study.

Acknowledgments

We are grateful to Warit Mitthumsiri and David Ruffolo for helpful comments and discussions. This research project is supported by the Thailand Research Fund (Grant TRG5880173).

References

[1] Jungman G, Kamionkowski M, and Griest M K 1996 *Phys. Rept.* **267** 195.
[2] Bertone G, Hooper D, and Silk J 2005 *Phys. Rept.* **405** 279.
[3] Zwicky F 1993 *Helvitica Phys.* **6** 110.
[4] Rubin V and Ford K 1970 *Astrophys. J.* **159** 379.
[5] Rubin V, Ford K, and Thonnard N 1980 *Journal of Modern Physics* **238** 471.
[6] Clowe D *et al.* 2006 *Astrophys. J.* **648** L109.
[7] Bradac M *et al.* 2006 *Astrophys. J.* **652** 937-947.
[8] Komatsu E *et al.* 2010 *Astrophys. J.* **192** 18.
[9] Bergstrom L 2009 Dark matter candidates *New. J. Phys.* **11** 105006.
[10] Cirelli M 2012 [arXiV: 1202.1454][hep-ph]
[11] Ackermann M *et al.* 2015 *Phys. Rev.* D. **91** 122002.
[12] Ibarra A and Tran D 2008 *Phys. Rev. Lett.* **100** 06103.
[13] Atwood W B *et al.* 2013 *2012 Fermi Symposium proceedings* eConf c121028.
[14] Ackermann M *et al.* 2013 *Phys. Rev.* D. **88** 082002.
[15] Wechakama M and Ascasibar Y 2014 *MNRAS* **439** 566-587.
[16] Abdo A A *et al* 2009 *Astrophys. J. Suppl.* **183** 46-66.